A HBc

B △ HBc

C Z_{HER2}-△HBc

Fig. 5 Relative fluorescence units (RFUs) of HER2 positive and negative cells treated with several concentrations of Alexa Fluor 488-labelled HBc core particles. RFUs were determined by FACS measurement. (A) HBc, (B) △HBc and (C) Z_{HER2}-△HBc. White bars, SKBR3 (HER2, +++); grey bars, MCF-7 (HER2, +) and black bars, HeLa (HER2, −).

HER2) and a HER2-negative human cervical cancer cell (HeLa) at several concentrations. After 3 h of incubation, we measured the fluorescence intensity of these cells by FACS.

As shown in Fig. 5A, the addition of a wild-type HBc particle caused a dose-dependent increase in fluorescence for all three kinds of cancer cells (SKBR3, MCF-7 and HeLa), indicating that the original HBc particle binds to the cells in a non-specific manner. The addition of a △HBc particle did not exhibit fluorescence for all three cells, supporting the theory that the deletion of the arginine-rich domain can cancel the non-specific binding ability of the original HBc (Fig. 5B). In contrast, the addition of a Z_{HER2}-△HBc particle promoted an apparent fluorescence for SKBR3 cells in a dose-dependent manner (white bars), whereas it never exhibited fluorescence for the HeLa cells (black bars) (Fig. 5C). Additionally, the addition of Z_{HER2}-△HBc to MCF-7 showed a weaker fluorescence than in the case of SKBR3 (Fig. 5C, grey bars). These results indicate that Z_{HER2}-△HBc specifically recognized HER2-expressing breast cancer cells and that the binding amount of Z_{HER2}-△HBc differed in accordance with the HER2 expression levels in the cells.

Finally, to visually observe the binding ability of these particles to the cells, Alexa Fluor 488-labelled core particles were added into the cell cultures (SKBR3, MCF-7 and HeLa) to give a final concentration of 10 μg/ml. After 3 h of incubation, the cells were observed using a confocal laser scanning microscope (Fig. 6). These results were consistent with the results of the FACS analyses (Fig. 5), demonstrating that the Z_{HER2}-△HBc particle has the ability to specifically bind to HER2-expressing breast cancer cells.

In conclusion, we developed a HBc particle displaying a Z_{HER2} affibody that specifically recognizes HER2-expressing breast cancer cells. It would be possible to incorporate drugs into Z_{HER2}-HBc particles by using the dissociation and association mechanism regulated by salt concentration (24) or urea denaturant (18), or by fusing peptidic drugs to C-terminal tail of core protein (22). By inserting other types of affibody
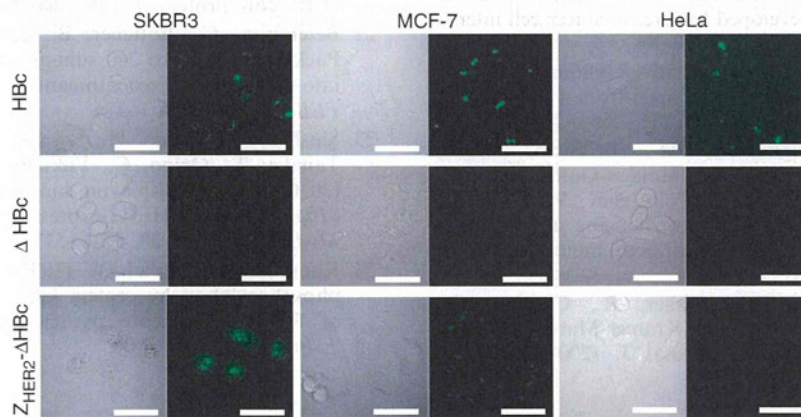

Fig. 6 Fluorescence images of SKBR3 (HER2, +++), MCF-7 (HER2, +) and HeLa (HER2, −) treated with Alexa Fluor 488-labelled HBc core particles (10 μg/ml). Cells were observed on a confocal laser scanning microscope. The fluorescence of Alexa Fluor 488 labeled HBc was shown in white. Scale bars, 50 μm.

255

molecules to the ΔHBc, these engineered HBc core particles could be used as pinpoint carriers to target various kinds of cancer cells.

Conflict of interest

None declared.

References

1. Wang, S., Placzek, W.J., Stebbins, J.L., Mitra, S., Noberini, R., Koolpe, M., Zhang, Z., Dahl, R., Pasquale, E.B., and Pellecchia, M. (2012) Novel targeted system to deliver chemotherapeutic drugs to EphA2-expressing cancer cells. *J. Med. Chem.* **55**, 2427–2436

2. Lorberboum-Galski, H. (2011) Human toxin-based recombinant immunotoxins/chimeric proteins as a drug delivery system for targeted treatment of human diseases. *Expert Opin. Drug Deliv.* **5**, 605–621

3. Liong, M., Lu, J., Kovochich, M., Xia, T., Ruehm, S.G., Nel, A.E., Tamanoi, F., and Zink, J.I. (2008) Multifunctional inorganic nanoparticles for imaging, targeting, and drug delivery. *ACS Nano.* **2**, 889–896

4. Nie, S., Xing, Y., Kim, G.J., and Simons, J.W. (2007) Nanotechnology applications in cancer. *Annu. Rev. Biomed. Eng.* **9**, 257–288

5. Ma, L.L., Tam, J.O., Willsey, B.W., Rigdon, D., Ramesh, R., Sokolov, K., and Johnston, K.P. (2011) Selective targeting of antibody conjugated multifunctional nanoclusters (nanoroses) to epidermal growth factor receptors in cancer cells. *Langmuir.* **27**, 7681–7690

6. Accardo, A., Salsano, G., Morisco, A., Aurilio, M., Parisi, A., Maione, F., Cicala, C., Tesauro, D., Aloj, L., Rosa, G.D., and Morelli, G. (2012) Peptide-modified liposomes for selective targeting of bombesin receptors overexpressed by cancer cells: a potential theranostic agent. *Int. J. Nanomed.* **7**, 2007–2017

7. Zhang, K., Sefah, K., Tang, L., Zhao, Z., Zhu, G., Ye, M., Sun, W., Goodison, S., and Tan, W. (2012) A novel aptamer developed for breast cancer cell internalization. *ChemMedChem.* **7**, 79–84

8. Nygren, P.-A. (2008) Alternative binding proteins: affibody binding proteins developed from a small three-helix bundle scaffold. *FEBS. J.* **275**, 2668–2676

9. Orlova, A., Magnusson, M., Eriksson, T.L.J., Nilsson, M., Larsson, B., Hoiden-Guthenberg, I., Widstrom, C., Carlsson, J., Tolmachev, V., Stahl, S., and Nilsson, F.Y. (2006) Tumor imaging using a picomolar affinity HER2 binding affibody molecule. *Cancer Res.* **66**, 4339–4348

10. Lee, S.B., Hassan, M., Fisher, R., Chertov, O., Chernomordik, V., Kramer-Marek, G., Gandjbakhche, A., and Capala, J. (2008) Affibody molecules for *in vivo* characterization of HER2-positive tumors by near-infrared imaging. *Clin. Cancer Res.* **14**, 3840–3849

11. Shojaei, S., Gardaneh, M., and Shamabadi, A.R. (2012) Target points in trastuzumab resistance. *Int. J. Breast Cancer* **2012**, 1–9

12. Gao, J., Chen, K., Miao, Z., Ren, G., Chen, X., Gambhir, S.S., and Cheng, Z. (2011) Affibody-based nanoprobes for HER2-expressing cell and tumor imaging. *Biomaterials.* **32**, 2141–2148

13. Puri, A., Kramer-Marek, G., Campbell-Massa, R., Yavlovich, A., Tele, S.C., Lee, S.B., Clogston, J.D., Patri, A.K., Blumenthal, R., and Capala, J. (2008) HER2-specific affibody-conjugated thermosensitive liposomes (Affisomes) for improved delivery of anticancer agents. *J. Liposome Res.* **18**, 293–307

14. Li, J., Lundberg, E., Vernet, E., Larsson, B., Hoiden-Guthenberg, I., and Graslund, T. (2010) Selection of affibody molecules to the ligand-binding site of the insulin-like growth factor-1 receptor. *Biotechnol. Appl. Biochem.* **55**, 99–109

15. Nordberga, E., Friedmanb, M., Gostringa, L., Adamsd, G.P., Brismare, H., Nilssona, F.Y., Stahlb, S., Glimeliusf, B., and Carlssona, J. (2007) Cellular studies of binding, internalization and retention of a radiolabeled EGFR-binding affibody molecule. *Nuc. Med. Bio.* **34**, 609–618

16. Cooper, A. and Shaul, Y. (2005) Recombinant viral capsids as an efficient vehicle of oligonucleotide delivery into cells. *BBRC.* **327**, 1094–1099

17. Leea, K.W. and Tana, W.S. (2008) Recombinant hepatitis B virus core particles: association, dissociation and encapsidation of green fluorescent protein. *J. Virol. Meth.* **151**, 172–180

18. Wizemann, H. and von Brunn, A. (1999) Purification of *E. coli*-expressed HIS-tagged hepatitis B core antigen by Ni^{2+}-chelate affinity chromatography. *J. Virol. Meth.* **77**, 189–197

19. Cooper, A. and Shaul, Y. (2006) Clathrin-mediated endocytosis and lysosomal cleavage of hepatitis B virus capsid-like core particles. *JBC* **281**, 16563–16569

20. Kratz, P.A., Bottcher, B., and Nassal, M. (1999) Native display of complete foreign protein domains on the surface of hepatitis B virus capsids. *PNAS* **96**, 1915–1920

21. Birnbaum, F. and Nassal, M. (1990) Hepatitis B virus nucleocapsid assembly: primary structure requirements in the core protein. *J. Virol.* **64**, 3319–3330

22. Beteramsa, G., Bottcher, B., and Nassal, M. (2000) Packaging of up to 240 subunits of a 17 kDa nuclease into the interior of recombinant hepatitis B virus capsids. *FEBS Lett.* **481**, 169–176

23. Shishido, T., Mieda, H., Hwang, S.Y., Nishimura, Y., Tanaka, T., Ogino, C., Fukuda, H., and Kondo, A. (2010) Affibody-displaying bionanocapsules for specific drug delivery to HER2-expressing cancer cells. *Bioorg. Med. Chem. Lett.* **20**, 5726–5731

24. Kann, M. and Gerlich, W. (1994) Effect of core protein phosphorylation by protein kinase C on encapsidation of RNA within core particles of hepatitis B virus. *J. Virol.* **68**, 7993–8000

Short communication

An affinity chromatography method used to purify His-tag-displaying bio-nanocapsules

Yuya Nishimura [a], Koichi Takeda [a], Jun Ishii [b], Chiaki Ogino [a], Akihiko Kondo [a,*]

[a] Department of Chemical Science and Engineering, Graduate School of Engineering, Kobe University, Japan
[b] Organization of Advanced Science and Technology, Kobe University, Japan

ABSTRACT

A bio-nanocapsule derived from the hepatitis B virus (HBV) is expected to be useful as a drug delivery system carrier. Because various types of bio-nanocapsules have been developed, a simple and versatile purification method for bio-nanocapsules would be useful. Therefore, this study was focused on establishing a simple purification method using affinity chromatography by inserting a histidine tag (His-tag) into a bio-nanocapsule. The method achieved a simple, one-step purification with a yield that was 2.5-fold higher than conventional ultracentrifugation, and thus would be a desirable alternative method for recombinant virus-like particle purification.

Crown Copyright © 2013 Published by Elsevier B.V. All rights reserved.

A bio-nanocapsule consisting of a hepatitis B surface antigen (HBsAg) and a lipid bilayer is a hollow virus-like particle (Kuroda et al., 1992) that has been studied as a carrier for drug delivery systems (Yamada et al., 2003). Since wild type bio-nanocapsules recognize specific hepatic cells, they are used as carriers to deliver drugs to hepatocarcinomas (Yamada et al., 2003). In the past, wild type bio-nanocapsules have also been altered into modified bio-nanocapsules that recognize other types of cells by replacing the hepatocyte recognition site in the pre-S region with other targeting molecules (Kasuya et al., 2008; Shishido et al., 2009a,b). For example, a Z_{HER2}-displaying bio-nanocapsule (Z_{HER2}-bio-nanocapsule) recognizes specific HER2-expressing cells that include breast cancer cells and ovarian cancer cells (Shishido et al., 2010). The Z_{HER2} is one of a type of affibodies that are the mutant proteins derived from the Z domain of Staphylococcal protein A and function as affinity ligands (Orlova et al., 2006; Lee et al., 2008). These wild type and altered bio-nanocapsules can be mass-produced in yeast cells (Kuroda et al., 1992; Shishido et al., 2010). Approaches using ultracentrifugation (Kuroda et al., 1992) or affinity chromatography combined with gel filtration (Kasuya et al., 2009) have been reported as methods for purification of the bio-nanocapsules from crude yeast extract. The advantage of the ultracentrifugation method is a general versatility, which is

available to purify both wild type bio-nanocapsules and altered bio-nanocapsules; and, therefore, it is used conventionally for the purification of bio-nanocapsules. However, the yield and degree of purification are often not high enough because the density gradient methods are laborious for the complete removal of foreign substances, and the relative number of required purification steps leads to a loss in target proteins and time consumption. However, the affinity chromatography method can provide high-yield, high-degree purification using procedures that are simple and brief. However, these methods have not been frequently used to purify bio-nanocapsules, because it was believed they were not applicable. This procedure commonly requires appropriate purification columns that depend on the types of produced bio-nanocapsules, such as a sulfated cellulofine column (for wild type bio-nanocapsule; Kasuya et al., 2009) or a porcine IgG column (for Z domain-displaying bio-nanocapsule; Kasuya et al., 2009), and often there is a failure to find a suitable affinity column. Thus, since both methods have advantages and disadvantages, a simple, versatile and high-recovery purification method that would be applicable to any bio-nanocapsule would be useful. Therefore, in the present study, an attempt was made to establish an affinity chromatography method to purify bio-nanocapsules using the His-tag that is a gold standard for protein purification (Sakamoto et al., 2010) by fusing genetically hexahistidine sequences (His6) to a targeting molecule substituted for the pre-S region within the bio-nanocapsule. This simple method of only inserting a His6-tag is expected to apply only to wild type and altered bio-nanocapsules. Therefore, this study was focused on investigating whether this method could be used to successfully purify

* Corresponding author at: Department of Chemical Science and Engineering, Graduate School of Engineering, Kobe University, 1-1 Rokkodaicho, Nada-ku, Kobe 657-8501, Japan. Tel.: +81 78 803 6196; fax: +81 78 803 6196.
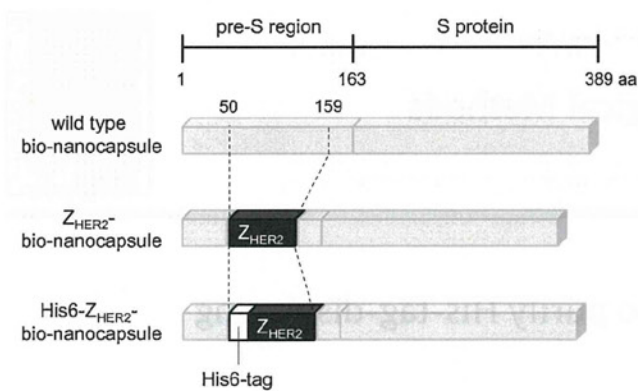E-mail address: akondo@kobe-u.ac.jp (A. Kondo).

Fig. 1. Schematic representations of constructed bio-nanocapsules (wild type bio-nanocapsule, Z_{HER2}-bio-nanocapsule and His6-Z_{HER2}-bio-nanocapsule).

Fig. 2. Analysis of the degree of purification by silver staining. Lanes 1–2, His6 affinity chromatography purification; lanes 3–8, ultracentrifugation purification. Sample was subjected to SDS-PAGE followed by crude yeast extract (lane 1 and lane 3) into an affinity column and dialyzed for 6 h (lane 2), PEG precipitation for 2 h (lane 4), dialysis for 6 h after CsCl ultracentrifugation for 16 h (lane 5), dialysis for 6 h after CsCl ultracentrifugation for 14 h (lane 6), dialysis for 6 h after sucrose ultracentrifugation for 10 h (lane 7) and condensation (lane 8).

Z_{HER2}-bio-nanocapsules using a His6-tag and its effectiveness was compared with that of the conventional ultracentrifugation purification method.

To purify bio-nanocapsules by His6 affinity chromatography, a plasmid that would express the His6-tagged Z_{HER2}-bio-nanocapsule in which His6 was fused to the N-terminus of a Z_{HER2} fragment (Fig. 1) was constructed. The plasmid for expression of the His6-tagged Z_{HER2}-bio-nanocapsule was constructed to replace the pre-S region in the L protein with a His6-Z_{HER2} molecule, as described below. The fragment encoding His6-fused Z_{HER2} (His6-Z_{HER2}) was amplified by polymerase chain reaction (PCR) using pGLDsLd50-Z_{HER2} (Shishido et al., 2010) as a template with the following primers: (5′-GGG GGA TCC CAC CAC CAC CAC CAC CAC GCG CAA CAC GAT GAA GCC GTA GAC AAC AAA TTC AAC AA-3′ and 5′-GGG GCG GCC GCC TTT CGG CGC CTA AGC ATC AT-3′). The amplified fragment was digested with *BamHI*/*NotI* and ligated into the *BamHI*/*NotI* sites of pGLDsLd50-Z_{HER2}. The resultant plasmid was designated as a pGLDsLd50-His6-Z_{HER2}. A *Saccharomyces cerevisiae* AH22R⁻ yeast strain was transformed with the constructed plasmid using the spheroplast method, and was cultured and disrupted with glass beads (Kuroda et al., 1992). Then the crude extract was examined as to whether it contained the His6-Z_{HER2} fusion proteins by western blotting using anti-His6 antibody and anti-protein A antibody (data not shown). Since the same sized bands were detected in both lanes, the produced bio-nanocapsules contained His6 and Z_{HER2} as a fusion protein.

A crude yeast extract was purified by each of the purification methods listed below. The degree of the purified samples collected in each step of purification was evaluated by silver staining using Sil-Best Stain One (Nacalai Tesque, Kyoto, Japan) (Fig. 2). The ultracentrifugation purification method was followed in accordance with the previous specified procedures (Kuroda et al., 1992). The objective bands were shown through five steps of purification, which contained polyethylene glycol (PEG) precipitation for 2 h (lane 4), dialysis for 6 h after CsCl ultracentrifugation for 16 h (lane 5), dialysis for 6 h after CsCl ultracentrifugation for 14 h (lane 6), dialysis for 6 h after sucrose ultracentrifugation for 10 h (lane 7), and condensation (lane 8). However, it was thought that the purified samples contained unnecessary proteins, because other thin bands and a smear band were also detected throughout the lanes.

Next, a His6 affinity chromatography method was performed as described below. The crude extract was prepared by disrupting the cultured yeast cells with glass beads in 75 ml of dissociation buffer [7.5 M Urea, 170 mM Na_2HPO_4, 40 mM NaH_2PO_4, 15 mM disodium ethylene diamine tetraacetic acid (EDTA/2Na), 2 mM phenylmethylsulfonyl fluoride (PMSF), and 0.01% sorbitan polyoxyethylene monooleate (Tween 80)]. The pellet was removed by centrifugation at $14,000 \times g$ and 4 °C for 10 min. The
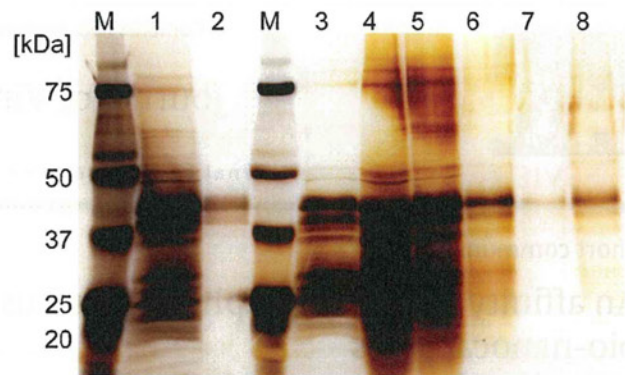
His6-Z_{HER2}-bio-nanocapsule was separated from the crude extract using Ni^{2+}-chelate affinity chromatography. A column with 5 ml of Ni^{2+}-chelate agarose (Nacalai Tesque) was pre-equilibrated with a 5-fold volume of dissociation buffer. The crude extract was loaded into the column and washed with 15 ml of dissociation buffer. Then, bound proteins were eluted with 15 ml of elution buffer (dissociation buffer with 1 M imidazole). The eluate was fractionated in 1 ml aliquots. The aliquots of each fraction were analyzed by silver staining to select the fractions containing proteins. The proteins of purified fractions were finally dialyzed in phosphate-buffered saline (PBS) to remove the urea. The method was very simple, and amounted to simply applying crude yeast extract into the affinity column and dialyzing it for 6 h (lane 2). Two objective, albeit different, bands were observed near 44 kDa that were produced by the presence and absence of N-glycosylation, as previously reported (Shishido et al., 2010). The thin band observed at near 25 kDa was a degraded His6-fused protein. This useless protein should be omitted by optimizing the process (e.g., changing the cultivation and/or extraction conditions) when the bio-nanocapsules are used for commercial purposes. Nevertheless, clear, objective bands were obtained without the smear bands produced by ultracentrifugation purification, demonstrating a high purity for the His6 affinity chromatography.

The collateral concentrations of proteins contained within each step of purification were measured using a Lowry protein assay and then the yields were calculated. In the case of the ultracentrifugation method (Table 1B), 1.3 mg protein (yield, 0.61%) was eventually obtained. When combined with the results of silver staining, however, the actual yield would be less than 0.61%. In the case of the His6 affinity chromatography method, 2.9 mg protein (yield, 1.52%) was eventually obtained. From the results of the silver staining, these values would be almost the same as the actual amount and yield of the His6-tagged target protein, because the useless proteins were rarely contaminated. As a result, the His6 affinity chromatography method achieved a yield that was almost 2.5-fold higher than that achieved with ultracentrifugation, despite being a simple one-step purification (Table 1A).

To evaluate the quality of purified His6-Z_{HER2}-bio-nanocapsules, the diameter was measured by DLS using a Zetasizer Nano particle size analyzer (Malvern Instruments, Worcestershire, UK). The His6-Z_{HER2}-bio-nanocapsules purified by His6 affinity chromatography were about 100 nm in diameter, and were similar to the His6-Z_{HER2}-bio-nanocapsules that were purified via the ultracentrifugation method. Since both diameters were almost equal to that

Table 1

The yield of purified protein for each step of (A) affinity chromatography method and (B) ultracentrifugation method. The number of steps was compatible with each lane of Fig.2.

(A)

Step of affinity chromatography method	Concentration [μg/ml]	Liquid measure [ml]	Mass [mg]	Yield [%]
1. Crude extract	2940.1	62.5	191.1	100.00
2. After affinity purification	189.9	15.0	2.9	1.52

(B)

Step of ultracentrifugation method	Concentration [μg/ml]	Liquid measure [ml]	Mass [mg]	Yield [%]
3. Crude extract	3566.9	60.0	214.0	100.00
4. After PEG precipitation	3461.8	27.0	93.5	43.69
5. After ultracentrifugation 1	522.1	55.0	28.7	13.41
6. After ultracentrifugation 2	154.2	47.5	7.3	3.41
7. After ultracentrifugation 3	28.0	103.8	2.9	1.36
8. After condensation	133.1	10.0	1.3	0.61

of the Z_{HER2}-bio-nanocapsules (without His6-tag) purified by the ultracentrifugation method (Shishido et al., 2010), this indicated that the insertion of a His6-tag into the Z_{HER2}-bio-nanocapsule had no influence on particle formation.

Finally, to determine the ability of cell specificity, the purified bio-nanocapsules were reacted with Alexa Fluor 488 succinimidyl esters (Invitrogen Life Technologies, Carlsbad, CA, USA) (2.6 mol equivalent) in PBS for 1 h at room temperature and the mixture was dialyzed against PBS overnight to remove the free Alexa Fluor 488. Then, the bio-nanocapsules were added to HER2-positive SKBR3 cells (human breast carcinoma) (Davison et al., 2011) and HER2-negative HeLa cells (human cervical carcinoma) (Jia et al., 2003). The fluorescence of the cells was observed using a confocal laser scanning microscope (CLSM) (Fig. 3). The fluorescence was observed in both SKBR3 cells treated with His6-Z_{HER2}-bio-nanocapsules purified by ultracentrifugation and the His6 affinity chromatography also with Z_{HER2}-bio-nanocapsules (without a His6-tag) purified by ultracentrifugation, which indicated that the His6-fused Z_{HER2}-bio-nanocapsules had no adverse effect on cell specificity. This result showed that the insertion of a His6-tag into the bio-nanocapsules is a successful alternate for the previously reported bio-nanocapsule purification techniques.

In conclusion, this study was successful in developing a simple, versatile and high-recovery purification method using His6 affinity chromatography. This method permits the basic purification of altered bio-nanocapsules, and would be useful for large-scale purification in commercial applications. Furthermore, this method could be applied uniformly to the purification of other recombinant virus-like particles, such as HIV-1 (Sakuragi et al., 2002), adeno-associated virus (Backovic et al., 2012) and dengue virus (Tang et al., 2012), which have been purified using the conventional ultracentrifugation method.

Acknowledgements

References

Backovic, A., Cervelli, T., Salvetti, A., Zentilin, L., Giacca, M., Galli, A., 2012. Capsid protein expression and adeno-associated virus like particles assembly in *Saccharomyces cerevisiae*. Microb. Cell Fact. 11, 124.

Davison, Z., Blacquiere, G.E., Westley, B.R., May, F.E.B., 2011. Insulin-like growth factor-dependent proliferation and survival of triple-negative breast cancer cells: implication for therapy. Neoplasia 13, 504–515.

Jia, L.T., Zhang, L.H., Yu, C.J., Zhao, J., Xu, Y.M., Gui, J.H., Jin, M., Ji, Z.L., Wen, W.H., Wang, C.J., Chen, S.Y., Yang, A.G., 2003. Specific tumoricidal activity of a secreted proapototic protein consisting of HER2 antibody and constitutively active caspase-3. Cancer Res. 63, 3257–3262.

Kasuya, T., Jung, J., Kadoya, H., Matsuzaki, T., Tatematsu, K., Okajima, T., Miyoshi, E., Tanizawa, K., Kuroda, S., 2008. In vivo delivery of bionanocapsules displaying *Phaseolus vulgaris* agglutinin-L₄ isolectin to malignant tumors overexpressing N-acetylglucosaminyltransferase V. Hum. Gene Ther. 19, 887–895.

Kasuya, T., Jung, J., Kinoshita, R., Goh, Y., Matsuzaki, T., Iijima, M., Yoshimoto, N., Tanizawa, K., Kuroda, S., 2009. Bio-nanocapsule–liposome conjugates for in vivo pinpoint drug and gene delivery. Methods Enzymol. 464, 147–166.

Kuroda, S., Otaka, S., Miyazaki, T., Nakao, M., Fujisawa, Y., 1992. Hepatitis B virus envelope L protein particles. Synthesis and assembly in *Saccharomyces cerevisiae*, purification and characterization. J. Biol. Chem. 267, 1953–1961.

Lee, S.B., Hassan, M., Fisher, R., Chertov, O., Chernomordik, V., Kramer-Marek, G., Gandjbakhche, A., Capala, J., 2008. Affibody molecules for in vivo characterization of HER2-positive tumors by near-infrared imaging. Clin. Cancer Res. 14, 3840–3849.

Orlova, A., Magnusson, M., Eriksson, T.L., Nilsson, M., Larsson, B., Hoiden-Guthenberg, I., Widstrom, C., Carlsson, J., Tolmachev, V., Stahl, S., Nilsson, F.Y., 2006. Tumor imaging using a picomolar affinity HER2 binding affibody molecule. Cancer Res. 66, 4339–4348.

Sakamoto., T., Sawamoto, S., Tanaka, T., Fukuda, H., Kondo, A., 2010. Enzyme-mediated site-specific antibody–protein modification using a ZZ domain as a linker. Bioconjugate Chem. 21, 2227–2233.

Sakuragi., S., Goto, T., Sano, K., Morikawa, Y., 2002. HIV type 1 Gag virus-like particle budding from spheroplasts of *Saccharomyces cerevisiae*. Proc. Natl. Acad. Sci. U.S.A. 99, 7956–7961.

Shishido, T., Azumi, Y., Nakanishi, T., Umetsu, M., Tanaka, T., Ogino, C., Fukuda, H., Kondo, A., 2009a. Biotinylated bionanocapsules for displaying diverse ligands toward cell-specific delivery. J. Biochem. 146, 867–874.

Shishido, T., Yonezawa, D., Iwata, K., Tanaka, T., Ogino, C., Fukuda, H., Kondo, A., 2009b. Construction of arginine-rich peptide displaying bionanocapsules. Bioorg. Med. Chem. Lett. 19, 1473–1476.
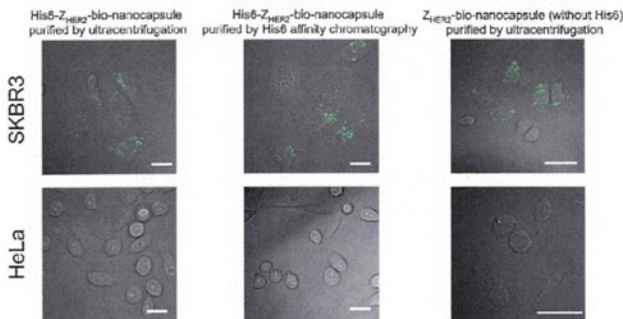

Fig. 3. Fluorescence images of HER2-positive SKBR3 and HER2-negative HeLa cells treated with Alexa Fluor 488 labeled His6-Z_{HER2}-bio-nanocapsule purified by ultracentrifugation or His6 affinity chromatography and Z_{HER2}-bio-nanocapsule (without His6) purified by ultracentrifugation. Cells were incubated for 1 h in the media adjusted to 10 μg/ml as protein. After washing twice, cells were additionally incubated for 2 h and then observed by a confocal laser scanning microscope. Scale bar, 50 μm.

Shishido, T., Mieda, H., Hwang, S.Y., Nishimura, Y., Tanaka, T., Ogino, C., Fukuda, H., Kondo, A., 2010. Affibody-displaying bionanocapsules for specific drug delivery to HER2-expressing cancer cells. Bioorg. Med. Chem. Lett. 20, 5726–5731.

Tang., Y.X., Jiang, L.F., Zhou, J.M., Yin, Y., Yang, X.M., Liu, W.Q., Fang, D.Y., 2012. Induction of virus-neutralizing antibodies and T cell responses by dengue virus type 1 virus-like particles prepared from Pichia pastoris. Chin. Med. J. (Engl.) 125, 1986–1992.

Yamada, T., Iwasaki, Y., Tada, H., Iwabuki, H., Chuah, M.K., VandenDriessche, T., Fukuda, H., Kondo, A., Ueda, M., Seno, M., Tanizawa, K., Kuroda, S., 2003. Nanoparticles for the delivery of genes and drugs to human hepatocytes. Nat. Biotechnol. 21, 885–890.

Inactivation of *Escherichia coli* by sonoelectrocatalytic disinfection using TiO$_2$ as electrode

Kazuaki Ninomiya [a], Masayuki Arakawa [b], Chiaki Ogino [c], Nobuaki Shimizu [a,*]

[a] *Institute of Nature and Environmental Technology, Kanazawa University, Kanazawa 920-1192, Japan*
[b] *Division of Material Engineering, Graduate School of Natural Science and Technology, Kanazawa University, Kanazawa 920-1192, Japan*
[c] *Department of Chemical Science and Engineering, Graduate School of Engineering, Kobe University, 1-1 Rokkodaicho, Nada-ku, Kobe 657-8501, Japan*

ABSTRACT

This is the first study to demonstrate sonoelectrocatalytic disinfection using titanium dioxide (TiO$_2$) as an anode for effective inactivation of *Escherichia coli*. In brief, a non-woven TiO$_2$ fabric used as an anode and a platinum cathode were immersed in an *E. coli* suspension in which a positive potential was applied to TiO$_2$ concomitant with ultrasound (US) irradiation. Two control experiments were performed using *E. coli* suspensions to exhibit the effects of the sonoelectrocatalytic disinfection. One was disinfection by applying a positive potential to a TiO$_2$ electrode, but without US irradiation (electrochemical disinfection). The other was disinfection without applying a potential, but with US irradiation in the presence of TiO$_2$ (sonocatalytic disinfection). The cell inactivation rate in sonoelectrocatalytic disinfection was synergistically much more enhanced than the combined inactivation rates in electrochemical disinfection and sonocatalytic disinfection. This synergistically enhanced inactivation rate of *E. coli* cells was attributable to effective reaction of the sonocatalytically generated OH radicals with *E. coli* cells at the surface of the TiO$_2$ anode, which resulted from the electroadsorption of *E. coli* cells toward the TiO$_2$ anode.

© 2012 Elsevier B.V. All rights reserved.

1. Introduction

Water treatments use various chemical and physical processes, such as ozonation and irradiation with γ-rays. Among these treatments, electrochemical disinfection has been given considerable attention because it is a simple and inexpensive method [1]. The mechanism for electrochemical disinfection and the degradation of organic pollutants are mainly categorized by two different oxidation reactions: (1) direct oxidation in which pollutants are oxidized at an anode surface by a direct electron transfer reaction between bacterial cells and the electrode; and (2) indirect oxidation in which oxidizing agents, such as HClO and reactive oxygen species (ROS), are electrochemically generated at the anode surface and destroy the pollutants [2,3].

Ultrasound (US) irradiation is also an efficient method for inactivation of bacteria and degradation of contaminants in water [4,5]. The mechanism underlying ultrasonic inactivation of bacterial cells is based on physical and chemical effects. US irradiation of water causes acoustic cavitations in which millions of small bubbles collapse to achieve temperatures as high as 5000 K and pressures as high as 100 MPa [6]. Such extreme conditions that occur when the bubbles collapse, result in generation of high-speed microjets

and highly active free hydroxyl (OH) radicals due to pyrolysis of water [7]. These physical and chemical factors inactivate bacterial cells. Recently, some papers reported on electrochemical disinfection used in conjunction with ultrasonic disinfection (sonoelectrochemical disinfection) [8].

Titanium dioxide (TiO$_2$) is a photocatalyst that generates ROS under ultraviolet (UV) irradiation [9]. ROS produced *via* photocatalytic reaction has been used for inactivation of bacteria as well as degradation of harmful chemicals in water [10]. Since Butterfield et al. first reported in 1997, there have been many reports on electrochemical disinfection in conjunction with photocatalytic disinfection using immobilized TiO$_2$ as an electrode and for photocatalysis (photoelectrocatalytic disinfection) [11–14]. However, when using a photocatalytic reaction with UV irradiation, problems arising from the turbidity of waste water are not resolved, which causes decrease in the efficiency of photocatalytic cell inactivation.

In a previous study, we discovered that TiO$_2$ can act as a sonocatalyst, i.e., the presence of TiO$_2$ particles enhanced OH radical generation during ultrasonic irradiation, even in the dark, without UV irradiation [15]. This sonocatalytic effect of TiO$_2$ particles has been applied to the degradation of chemicals [16–19] and the inactivation of bacteria such as *Escherichia coli* and *Legionella pneumophila* [20–24]. TiO$_2$ enhances ultrasonic disinfection by promoting the physical and chemical effects of US [25]. TiO$_2$ particles act as additional nuclei that increase cavitation bubbles, resulting

* Corresponding author. Tel.: +81 76 234 4807; fax: +81 76 234 4829.
E-mail address: nshimizu@t.kanazawa-u.ac.jp (N. Shimizu).

763

in extremely high temperatures and pressures when the bubbles collapse [26]. These conditions promote the generation of microjets and OH radicals. Moreover, thermal excitation of TiO_2 by extremely high temperatures [27,28] and photoexcitation of TiO_2 by sonoluminescence [29], resulting from the cavitation bubble implosions, leads to the generation of OH radicals. However, to date, no study has reported on electrochemical disinfection in conjunction with sonocatalytic disinfection using TiO_2.

Therefore, to develop a more efficient disinfection process, we demonstrated "sonoelectrocatalytic disinfection using TiO_2" which is a combination of electrochemical disinfection using TiO_2 as a working electrode and sonocatalytic disinfection using TiO_2 as a sonocatalyst, i.e., disinfection by applying potential to the TiO_2 electrode in conjunction with US irradiation to a bacterial suspension in the presence of TiO_2. To evaluate the efficacy of the sonoelectrocatalytic disinfection using TiO_2, inactivation of E. coli was examined. Moreover, membrane damage in E. coli cells was also examined to understand the cellular processes leading to cell death during sonoelectrocatalytic disinfection using TiO_2.

2. Materials and methods

2.1. Materials

Non-woven TiO_2 fabrics (Yield Co., Ltd., Kyoto, Japan), measuring 1.5×3.5 cm^2, were used as anodes for sonoelectrochemical disinfection. A pure non-woven titanium (Ti) fabric of the same size was also used as control, when necessary. The non-woven TiO_2 fabrics were prepared by direct oxidation of a pure non-woven Ti fabric by a previously described method [24]. Platinum plate (1.5×1.5 cm^2) was used as the cathode. The non-woven TiO_2 fabrics were cleaned ultrasonically and sterilized in a steam autoclave at 121 °C for 15 min prior to use. All chemicals used in this study were reagent grade, and laboratory grade water was prepared with an ultrapure water system.

2.2. Medium and microbial culture

Escherichia coli (NOVABlue™, Novagen Co. Ltd.) was used for this study. A single colony of E. coli was isolated after culture on a Luria Bertani (LB) agar plate (10 g/l tryptone, 5 g/l yeast extract, 5 g/l sodium chloride, and 15 g/l dextrose agar) and inoculated into a 300-ml baffled Erlenmeyer flask containing 100 ml of LB liquid media. The flask was incubated for 12 h at 37 °C on an orbital shaker at 140 rpm. After incubation, the culture broth was centrifuged at 3000 rpm for 10 min and washed twice with 100 mM phosphate buffer solution (pH = 7.0), which was used as the electrolyte in the sonoelectrocatalytic disinfection experiments. E. coli cells were diluted with the phosphate buffer solution to adjust the cell concentration to approximately 10^8 CFU/ml for the disinfection and microscopy experiments.

2.3. Sonoelectrocatalytic disinfection

Fig. 1 shows the experimental setup for the sonoelectrocatalytic disinfection. A non-woven TiO_2 fabric (working electrode) and platinum (counter electrode) were placed in parallel and separated by 20 mm in a Pyrex glass reaction vessel (diameter, 30 mm; volume, 50 ml) containing 10 ml of E. coli suspension in the electrolyte. Chloride-free phosphate buffer solution was used as the electrolyte to eliminate the generation of chlorine species such as HClO. The top of the electrodes were connected to a constant current device (SEN7103 equipped with SS102J, Nihon Kohden Co., Tokyo, Japan); the applied constant current was 10 mA. The reaction vessel was set in the center of a US bath (UO 300 FB-P;
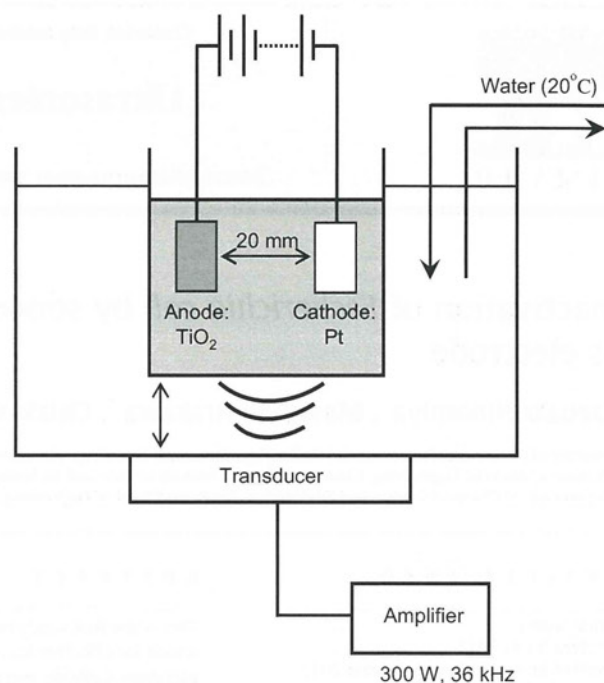

Fig. 1. Diagram of the experimental apparatus for sonoelectrocatalytic disinfection. The anode and cathode are a non-woven TiO_2 fabric (1.5×3.5 cm^2) and a Pt electrode (1.5×1.5 cm^2), respectively.

Kokusai Alpha Co. Ltd., Toyama, Japan; working volume: 5.8 l), which was set at an operating frequency of 36 kHz. The US power delivered to the sample was determined by a calorimetric method [30], which was calculated as 0.28 W [24]. The water temperature in the US bath was maintained at 20 ± 0.5 °C by connecting a circulator. Sonoelectrocatalytic disinfection was performed in the dark by covering the bath, and the reaction vessel was covered with aluminum foil before and after disinfection to eliminate the effects of illumination. During disinfection, samples (200 µl each) were withdrawn carefully and used to evaluate the viable cell concentration and cell membrane integrity.

To emphasize the unique characteristics of sonoelectrocatalytic disinfection, two control experiments were performed. One was disinfection by applying a positive potential alone to the TiO_2 electrode, but without US irradiation (called electrochemical disinfection here). The other was disinfection without applying a potential, but with US irradiation of E. coli suspension in the presence of TiO_2 (called sonocatalytic disinfection in the present study). In some experiments, 30 mM of t-butanol (Sigma, St. Louis, MO, USA) was also added to the reaction vessel as an OH radical scavenging agent.

2.4. Observation of electroadsorption of E. coli

To directly observe the electroadsorption behavior of E. coli cells toward TiO_2 anode, electrophoresis of the cells was continuously monitored using a microscope. Here, E. coli strain expressing green fluorescent protein (GFP) was used for easy tracking using a fluorescence microscopy. The E. coli strain was prepared by introducing the plasmid pQBI-T7-GFP (qBiogene, Inc. Irvine, CA, USA) and inducing protein expression by adding isopropylthio-β-galactoside according to the standard protocol. The non-woven TiO_2 fabric and platinum electrodes were immersed in parallel and separated by 20 mm in a petri dish containing the prepared E. coli cells suspended in phosphate buffer solution. A positive potential was

applied to TiO_2 against the counter electrode as described above. Petri dish was placed on the stage of inverted microscope and fluorescent microscopy images were acquired at prescribed time intervals.

2.5. Analyses of cell viability and cell membrane integrity

To evaluate the cell viability, a withdrawn sample was diluted appropriately and plated on LB agar plates. After incubation for 12 h at 37 °C, the viable cell concentration (N) was evaluated based on CFU/ml. Cell survival ratio was calculated as N/N_0, where N_0 was the viable cell concentration before disinfection.

To evaluate the cytoplasmic membrane integrity of the E. coli cells, propidium iodide (PI) (Nacalai tesque, Inc., Kyoto, Japan) was used. PI is impermeable across the cytoplasmic membrane and is excluded from viable cells, although it exhibits enhanced fluorescence once it binds to intercellular nucleic acids. PI was added to a withdrawn sample at a final concentration of 60 µM and incubated on ice for 10 min in the dark. The fluorescence intensity of stained E. coli sample (F) was measured using fluorescence plate reader (Cytofluor 4000; Applied Biosystems, Foster City, CA, USA) with a wavelength of 530 nm for excitation and 645 nm for emission. Changes in fluorescence intensity (ΔF) were calculated as the difference between the F value for the described disinfection condition and that for the control condition without an applied potential or US irradiation.

3. Results and discussion

3.1. Bacterial cell inactivation by sonoelectrocatalytic disinfection

Fig. 2 shows the time course of the E. coli cell survival ratios during disinfection with applying a positive potential to the TiO_2 electrode and/or irradiating US. Without an applied potential or US irradiation, there was no decline in the cell survival ratio, even though the TiO_2 electrode was present. When only a potential was applied to the TiO_2 electrode immersed in an E. coli suspension (electrochemical disinfection), a slight decrease in the cell survival

ratio was observed; the N/N_0 value was 0.65 at 60 min of disinfection. When only US irradiation of the TiO_2 electrode was used (sonocatalytic disinfection), the decrease in the cell survival ratio was more significant; the N/N_0 value was 0.12 at 60 min of disinfection. When a potential was applied to the TiO_2 electrode in conjunction with US irradiation to the E. coli suspension (sonoelectrocatalytic disinfection), the cell inactivation rate was synergistically much more enhanced than the combined inactivation rates in electrochemical disinfection and sonocatalytic disinfection, where the N/N_0 value was 0.012 at 60 min of disinfection.

In electrochemical disinfection (open triangles in Fig. 2), E. coli cells were adsorbed to a positively charged anode because of an electroattractive interaction between bacterial cells and the anode because the surface charge of the E. coli cell wall was negative in a wide range of solutions including phosphate buffer solution (pH = 7) [31]. Although the surface electric charge of TiO_2 was originally negative at pH 7 [32], the electroadsorption behavior of E. coli cells toward the positively charged TiO_2 anode was confirmed by direct monitoring using fluorescence microscopy (Fig. 3 and video data in Supplementary information). Moreover, E. coli cells were inactivated by direct oxidation at the surface of the TiO_2 anode and by indirect oxidation because of ROS generated at the TiO_2 surface. The lifetime of ROS is so short that oxidation of E. coli cells by ROS primarily occurred at the anode surface and not in the bulk phase. Chlorine species, such as HClO, which shows relatively longer lifetime and works in the bulk phase, was not formed in this study because a chloride-free phosphate buffer
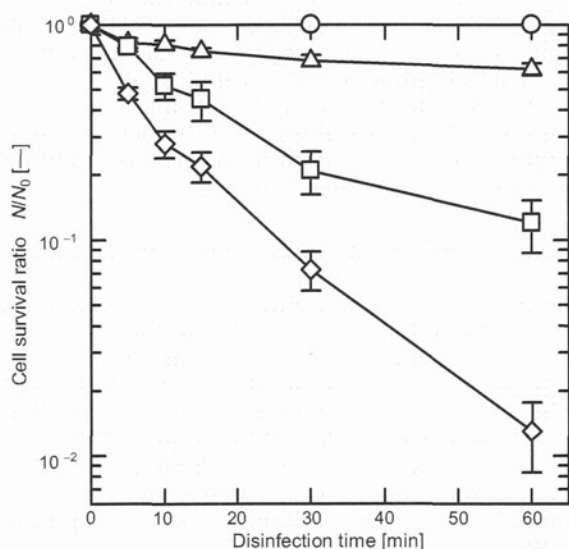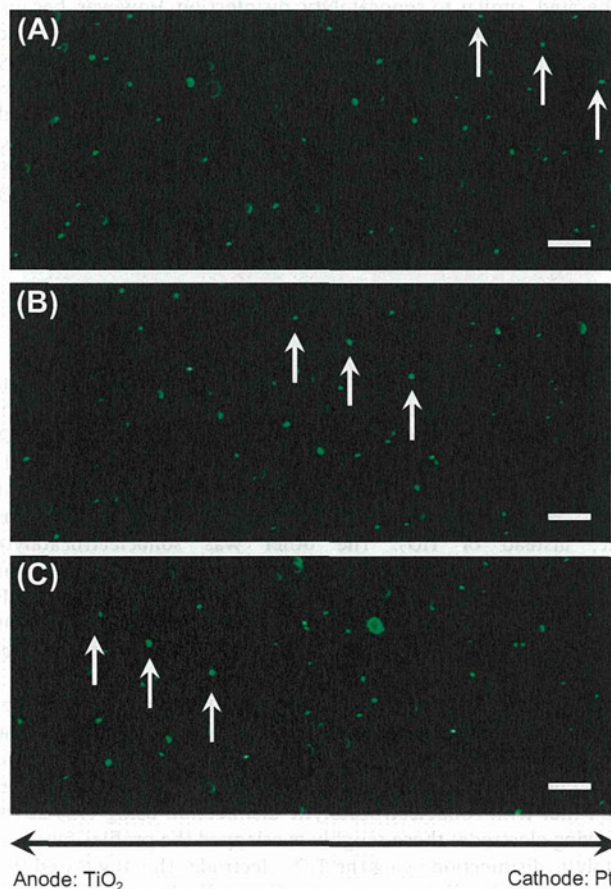

Fig. 2. Time course for the E. coli cell survival ratios during electrochemical, sonocatalytic, and sonoelectrocatalytic disinfection. Open circles: control; open triangles: electrochemical disinfection; open squares: sonocatalytic disinfection; and open diamonds: sonoelectrocatalytic disinfection. Results are the means of five independent experiments. Error bars indicate standard errors.

Fig. 3. Movement of E. coli cells towards the TiO_2 anode during application of a constant current (10 mA). Fluorescent microscopic images are of E. coli cells that express GFP. A, B, and C are time series images acquired at intervals of 2.3 s. Arrows in each image indicate the same E. coli cells. Horizontal bars = 10 µm.

solution was used as the electrolyte. Therefore, *E. coli* cells were adsorbed and inactivated mainly at the surface of the TiO_2 electrode in electrochemical disinfection employed in the study. However, the cell inactivation rate itself was quite low compared with that examined at other conditions.

During sonocatalytic disinfection using TiO_2 (open squares in Fig. 2), disinfection occurred both in the bulk phase and at the TiO_2 surface. In the bulk phase, *E. coli* cells were inactivated by the microjet shear stress and the OH radicals generated under US irradiation. Moreover, at the surface of the TiO_2 electrode, *E. coli* cells were inactivated by OH radicals generated by sonocatalytic excitation of TiO_2. In our previous study, the amount of OH radicals that were generated by sonocatalytic excitation of TiO_2 was significantly greater than the amount generated by US irradiation alone [26]. However, in the sonocatalytic disinfection using the TiO_2 electrode employed in this study, TiO_2 was not suspended as particles but was immobilized as an electrode and could not disperse in the bulk phase. Moreover, there was no electroattractive interaction between the TiO_2 anode and *E. coli* cells as the surfaces of both TiO_2 and *E. coli* cells were negatively charged in the phosphate buffer solution (pH = 7). Therefore, the sonocatalytically generated OH radicals at the surface of the TiO_2 anode could not be effectively utilized to inactivate *E. coli* cells during its lifetime.

In the sonoelectrocatalytic disinfection using TiO_2 as electrode (open diamonds in Fig. 2), direct and indirect oxidation of *E. coli* cells took place at the surface of TiO_2 electrode, similar to electrochemical disinfection. Simultaneously, *E. coli* cells were inactivated in the bulk phase by the microjet shear stress and the OH radicals generated, similar to sonocatalytic disinfection. However, because of the applied potential to the TiO_2 electrode, electroadsorption of *E. coli* cells toward TiO_2 anode surface was expected, which accelerated the *E. coli* inactivation by the sonocatalytically generated OH radicals at the surface of the TiO_2 anode. Thus, it was considered that synergistically enhanced inactivation rate in the sonoelectrocatalytic process was attributable to the effective cell killing by the sonocatalytically generated OH radicals at the TiO_2 anode surface which was due to attractive interaction between TiO_2 anode and *E. coli* cells.

3.2. Validation of the synergistically enhanced cell inactivation by sonoelectrocatalytic disinfection

As described in the previous section, the synergistically enhanced cell inactivation during sonoelectrocatalytic disinfection was attributed to the electroadsorption of *E. coli* cells to the TiO_2 anode surface, which sonocatalytically generated OH radicals. To verify this assumption, we performed two more control experiments. One was sonoelectrochemical disinfection using Ti as an anode, instead of TiO_2. The other was sonoelectrocatalytic disinfection by applying a negative potential to TiO_2. In these control experiments, *E. coli* cells were adsorbed to the Ti anode and Pt anode, respectively, which did not sonocatalytically generate OH radicals at their surfaces. Thus, these control experiments excluded the assumed cause of the synergistic effect.

The filled symbols in Fig. 4 indicate the time course for the cell survival ratios during sonoelectrochemical disinfection using Ti as anode and sonoelectrocatalytic disinfection using TiO_2 as a counter electrode. In both cases, the cell inactivation profile was slower than that with sonoelectrocatalytic disinfection using TiO_2 as the working electrode; these roughly overlapped the profiles for sonocatalytic disinfection using the TiO_2 electrode. This suggested that the disinfection efficiency was not synergistic, but was simply the sum of electrochemical disinfection and sonocatalytic disinfection using the TiO_2 electrode. Based on the results of these control experiments, it was confirmed that the reason why sonoelectrocatalytic disinfection exhibited a synergistically enhanced inactiva-
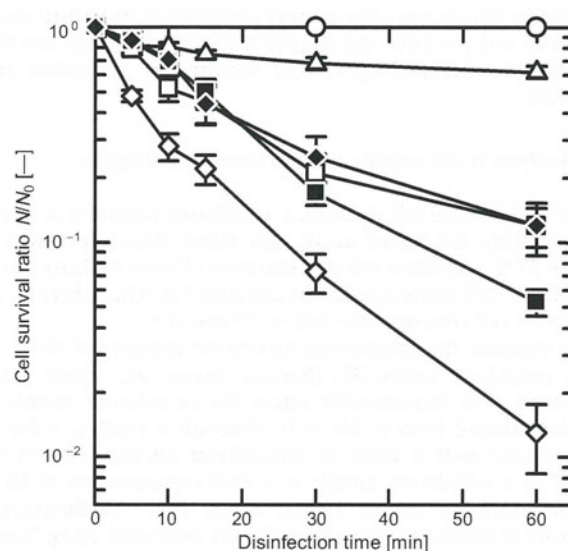

Fig. 4. Time course for the *E. coli* cell survival ratios during control disinfection experiments with sonoelectrocatalytic disinfection using a TiO_2 anode. Filled diamonds: control sonoelectrocatalytic experiment when Ti was used as the anode in place of TiO_2; filled squares: control sonoelectrocatalytic experiment when applying a negative potential to the TiO_2 electrode. Other results are for the same conditions as in Fig. 2 (Open circles: control experiment; open triangles: electrochemical disinfection; open squares: sonocatalytic disinfection; and open diamonds: sonoelectrocatalytic disinfection). Results are the means of five independent experiments. Error bars indicate standard errors.

tion rate was that the sonocatalytically generated OH radicals could react with *E. coli* cells at the TiO_2 anode, which resulted from the electroadsorption of *E. coli* cells to the TiO_2 anode surface.

3.3. Contribution of OH radicals to sonoelectrocatalytic disinfection

To check the contribution of OH radicals on cell inactivation during sonoelectrocatalytic disinfection, *t*-butanol was employed as an OH radical-scavenging agent. Fig. 5 shows the time course for the cell survival ratios during electrochemical, sonocatalytic, and sonoelectrocatalytic disinfection after addition of 30 mM *t*-butanol. Regardless of the method used, the disinfection rate was slightly reduced by the addition of *t*-butanol compared with the control experiments, wherein OH radical was used as a scavenging agent. Thus, this suggested that OH radicals contributed to the electrochemical, sonocatalytic, and sonoelectrocatalytic disinfection methods examined in this study.

3.4. Effects of sonoelecatalytic disinfection on membrane of E. coli cells

We considered that there were three lethal mechanisms involved in sonoelectrocatalytic disinfection. The first was direct electron transfer from the cells to the electrode surface induced electrochemically, where the cellular constituents are oxidized and the cell membrane is irreversibly permeabilized [33]. The second was shear stress in the bulk phase due to the collapse of cavitation bubbles that were generated ultrasonically, in which case the cell membrane was ruptured. The third was oxidation due to ROS in the bulk phase generated ultrasonically and ROS at TiO_2 anode surface generated electrochemically and sonocatalytically, in which case the cell membrane injury was caused by a membrane lipid peroxidation reaction [24,34]. Thus, the cell membrane injury was probably common and the first process that would result in cell death during sonoelectrocatalytic disinfection. Therefore, we examined injury to the outer cell membranes and the cytoplasmic
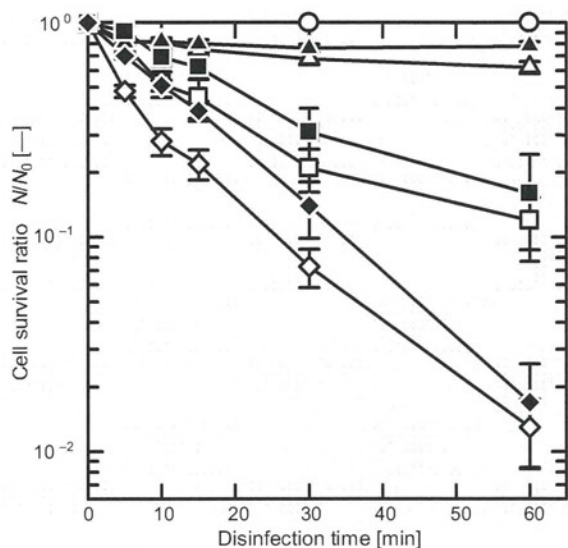
Fig. 5. Time course for the *E. coli* cell survival ratios during electrochemical, sonocatalytic, and sonoelectrocatalytic disinfection after adding a OH radical scavenging agent. Open and filled symbols are disinfection in the absence and presence of the OH radical scavenging agent (30 mM *t*-butanol), respectively. Symbols are as in Fig. 2 (Circles: control experiment; triangles: electrochemical disinfection; squares: sonocatalytic disinfection; and diamonds: sonoelectrocatalytic disinfection). Results are the means of five independent experiments. Error bars indicate standard errors.
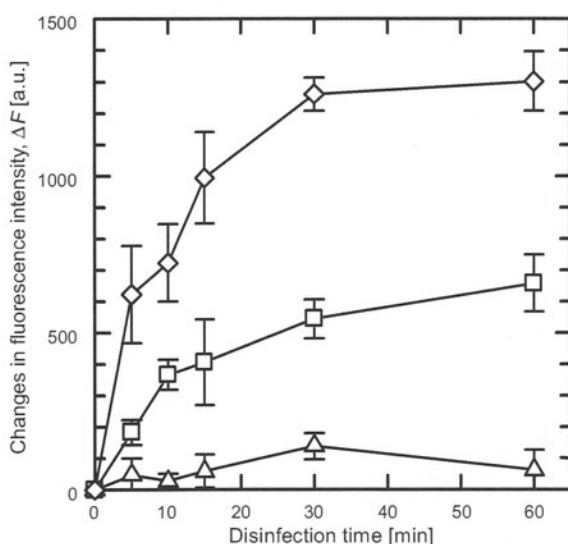
Fig. 6. Changes in fluorescence intensity of *E. coli* cells stained with PI during electrochemical, sonocatalytic, and sonoelectrocatalytic disinfection. Symbols are as in Fig. 2 (Open triangles: electrochemical disinfection; open squares: sonocatalytic disinfection; and open diamonds: sonoelectrocatalytic disinfection). Results are the means of five independent experiments. Error bars indicate standard errors.

membranes of *E. coli* cells during disinfection. Fig. 6 shows the time course for the fluorescence intensities of PI-stained *E. coli* samples that were withdrawn during electrochemical, sonocatalytic, and sonoelectrocatalytic disinfection. The fluorescence signals derived from PI were indices of injuries to the cytoplasmic membranes of *E. coli* cells. The fluorescent signals were highest with sonoelectrocatalytic disinfection, followed by sonocatalytic and electrochemical disinfection. Moreover, the fluorescence signal in sonoelectrocatalytic disinfection was synergistically much more enhanced than the combined data in electrochemical disinfection

and sonocatalytic disinfection. These results were consistent with the disinfection trends shown in Fig. 2, which indicated that cell membrane injury was the main lethal mechanism against *E. coli* cells for these disinfection methods.

4. Conclusions

In conclusion, sonoelectrocatalytic disinfection by applying potential to the TiO₂ electrode in conjunction with US irradiation of *E. coli* suspension synergistically enhanced the cell inactivation rate compared with the combined inactivation rates in electrochemical disinfection using the TiO₂ electrode and sonocatalytic disinfection in the presence of a TiO₂ sonocatalyst. Sonoelectrocatalytic disinfection had a synergistically enhanced inactivation rate because sonocatalytically generated OH radicals at the surface of the TiO₂ anode could be effectively utilized to inactivate *E. coli* cells as a result of the electroadsorption of *E. coli* cells toward the TiO₂ anode.
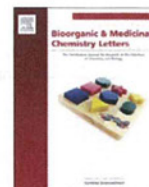
Appendix A. Supplementary data

Supplementary data associated with this article can be found, in the online version, at http://dx.doi.org/10.1016/j.ultsonch.2012.10.007.

References

[1] G.E. Stoner, G.L. Cahen, M. Sachyani, E. Gilbadi, The mechanism of low frequency a.c. electrochemical disinfection, Bioelectrochem. Bioenerg. 9 (1982) 229–243.
[2] A. Ánglada, A. Urtiaga, I. Ortiz, Contributions of electrochemical oxidation to waste-water treatment: fundamentals and review of applications, J. Chem. Technol. Biotechnol. 84 (2009) 1747–1755.
[3] J. Jeong, J.Y. Kim, J. Yoon, The role of reactive oxygen species in the electrochemical inactivation of microorganisms, Environ. Sci. Technol. 40 (2006) 6117–6122.
[4] P. Piyasena, Inactivation of microbes using ultrasound: a review, Int. J. Food Microbiol. 87 (2003) 207–216.
[5] P. Chowdhury, T. Viraraghavan, Sonochemical degradation of chlorinated organic compounds, phenolic compounds and organic dyes – a review, Sci. Total Environ. 407 (2009). 2474-292.
[6] K.S. Suslick, Sonochemistry, Science 247 (1990) 1439–1445.
[7] K.S. Suslick, The chemical effects of ultrasound, Sci. Am. 260 (1989) 80–86.
[8] E. Joyce, T.J. Mason, S.S. Phull, J.P. Lorimer, The development and evaluation of electrolysis in conjunction with power ultrasound for the disinfection of bacterial suspensions, Ultrason. Sonochem. 10 (2003) 231–234.
[9] A. Fujishima, K. Honda, Electrochemical photolysis of water at a semiconductor electrode, Nature 238 (1972) 37–38.
[10] A. Fujishima, T.N. Rao, D.A. Tryk, Titanium dioxide photocatalysis, J. Photochem. Photobiol. 1 (2000) 1–21.
[11] I.M. Butterfield, P.A. Christensen, T.P.J. Curtis, Gunlazuardi, Water disinfection using an immobilized titanium dioxide film in a photochemical reactor with electric field enhancement, Water Res. 31 (1997) 675–677.
[12] N. Baram, D. Starosvetsky, J. Starosvetsky, M. Epshtein, R. Armon, Y. Ein-Eli, Enhanced inactivation of *E. coli* bacteria using immobilized porous TiO₂ photoelectrocatalysis, Electrochim. Acta 54 (2009) 3381–3386.
[13] N. Philippidis, E. Nikolakaki, S. Sotiropoulos, I. Poulios, Photoelectrocatalytic inactivation of *E. coli* XL-1 blue colonies in water, J. Chem. Technol. Biotechnol. 85 (2010) 1054–1060.
[14] M. Cho, E.L. Cates, J.-H. Kim, Inactivation and surface interactions of MS-2 bacteriophage in a TiO₂ photoelectrocatalytic reactor, Water Res. 45 (2011) 2104–2110.
[15] N. Shimizu, C. Ogino, M.F. Dadjour, K. Ninomiya, A. Fujihira, K. Sakiyama, Sonocatalytic facilitation of hydroxyl radical generation in the presence of TiO₂, Ultrason. Sonochem. 15 (2008) 988–994.
[16] A.B. Pandit, P.R. Gogate, S. Mujumdar, Ultrasonic degradation of 2:4:6 trichlorophenol in presence of TiO₂ catalyst, Ultrason. Sonochem. 8 (2001) 227–231.

[17] J. Wang, B. Guo, X. Zhang, Z. Zhang, J. Han, J. Wu, Sonocatalytic degradation of methyl orange in the presence of TiO₂ catalysts and catalytic activity comparison of rutile and anatase, Ultrason. Sonochem. 12 (2005) 331–337.

[18] M. Kubo, K. Matsuoka, A. Takahashi, N. Shibasaki-Kitakawa, T. Yonemoto, Kinetics of ultrasonic degradation of phenol in the presence of TiO₂ particles, Ultrason. Sonochem. 12 (2005) 263–269.

[19] N. Shimizu, C. Ogino, M.F. Dadjour, T. Murata, Sonocatalytic degradation of methylene blue with TiO₂ pellets in water, Ultrason. Sonochem. 14 (2007) 184–190.

[20] M. Kubo, R. Onodera, N. Shibasaki-Kitakawa, K. Tsumoto, T. Yonemoto, Kinetics of ultrasonic disinfection of Escherichia coli in the presence of titanium dioxide particles, Biotechnol. Prog. 21 (2005) 897–901.

[21] M. Dadjour, C. Ogino, S. Matsumura, N. Shimizu, Kinetics of disinfection of by catalytic ultrasonic irradiation with TiO₂, Biochem. Eng. J. 25 (2005) 243–248.

[22] C. Ogino, M.F. Dadjour, K. Takaki, N. Shimizu, Enhancement of sonocatalytic cell lysis of Escherichia coli in the presence of TiO₂, Biochem. Eng. J. 32 (2006) 100–105.

[23] M.F. Dadjour, C. Ogino, S. Matsumura, S. Nakamura, N. Shimizu, Disinfection of Legionella pneumophila by ultrasonic treatment with TiO₂, Water Res. 40 (2006) 1137–1142.

[24] M.M. Rahman, K. Ninomiya, C. Ogino, N. Shimizu, Ultrasound-induced membrane lipid peroxidation and cell damage of Escherichia coli in the presence of non-woven TiO₂ fabrics, Ultrason. Sonochem. 17 (2010) 738–743.

[25] N. Shimizu, K. Ninomiya, C. Ogino, M.M. Rahman, Potential uses of titanium dioxide in conjunction with ultrasound for improved disinfection, Biochem. Eng. J. 48 (2010) 416–423.

[26] N.H. Ince, R. Belen, Aqueous phase disinfection with power ultrasound: process kinetics and effect of solid catalysts, Environ. Sci. Technol. 35 (2001) 1885–1888.

[27] J. Mizuguchi, T. Shinbara, Disposal of used optical disks utilizing thermally-excited holes in titanium dioxide at high temperatures: a complete decomposition of polycarbonate, J. Appl. Phys. 96 (2004) 3514–3519.

[28] T. Shinbara, T. Makino, K. Matsumoto, J. Mizuguchi, Complete decomposition of polymers by means of thermally generated holes at high temperatures in titanium dioxide and its decomposition mechanism, J. Appl. Phys. 98 (2005) 044909.

[29] H. Ogi, M. Hirao, M. Shimoyama, Activation of TiO₂ photocatalyst by single-bubble sonoluminescence for water treatment, Ultrasonics 40 (2002) 649–650.

[30] T.J. Mason, P. Lorimer, M. Bates, Quantifying sonochemistry: casting some light on a "black art", Ultrasonics 30 (1992) 40–42.

[31] Y. Oren, H. Tobias, A. Soffer, Removal of bacteria from water by electroadsorption, Bioelectrochem. Bioenerg. 156 (1983) 347–351.

[32] C. Sentein, B. Guizard, S. Giraud, C. Yé, F. Ténégal, Dispersion and stability of TiO₂ nanoparticles synthesized by laser pyrolysis in aqueous suspensions, J. Phys. 170 (2009) 012013.

[33] K. Drees, M. Abbaszadegan, Comparative electrochemical inactivation of bacteria and bacteriophage, Water Res. 37 (2003) 2291–2300.

[34] P.C. Maness, S. Smolinski, D.M. Blake, Z. Huang, E.J. Wolfrum, W.A. Jacoby, Bactericidal activity of photocatalytic TiO₂ reaction: toward an understanding of its killing mechanism, Appl. Environ. Microbiol. 65 (1999) 4094–4098.

Contents lists available at SciVerse ScienceDirect

Bioorganic & Medicinal Chemistry Letters

Cell-SELEX based selection and characterization of DNA aptamer recognizing human hepatocarcinoma

Kazuaki Ninomiya [a], Kazuhiko Kaneda [b], Satoshi Kawashima [b], Yusuke Miyachi [c], Chiaki Ogino [c], Nobuaki Shimizu [a,*]

[a] Institute of Nature and Environmental Technology, Kanazawa University, Kakuma-machi, Kanazawa 920-1192, Japan
[b] Division of Material Engineering, Graduate School of Natural Science and Technology, Kanazawa University, Kakuma-machi, Kanazawa 920-1192, Japan
[c] Department of Chemical Science and Engineering, Graduate School of Engineering, Kobe University, 1-1 Rokkodaicho, Nada-ku, Kobe 657-8501, Japan

ARTICLE INFO

ABSTRACT

Single-stranded DNA aptamers recognizing human hepatocarcinoma were isolated by means of a systematic evolution of ligands by exponential enrichment using whole cells as targets (cell-SELEX). After 11 rounds of cell-SELEX procedure using human hepatoma HepG2 cells as targets and human normal hepatocyte cells as counterparts, 12 independent DNA aptamer candidate sequences were obtained. The specific interaction between selected DNA aptamers and targeted cell was confirmed. Dissociation constants of the 12 sequences obtained were also estimated in the range of 19–450 nM. Moreover, the consensus secondary structure was found in the isolated aptamers, which was responsible to the recognition of HepG2 cells.

Aptamers are single-stranded oligonucleotides (ssDNA or RNA) capable of binding to target molecules with high affinity and specificity[1,2] due to their tertiary structures.[3] Aptamers have the following attractive features as molecular probes compared with that of conventional antibodies:[4,5] low molecular weight, quick and reproducible synthesis, easy modification, long-term stability, low toxicity, low immunogenicity, and fast tissue penetration. These advantages have made aptamers an excellent alternative as molecular probes for clinical applications.[6,7] Aptamers are selected from random ssDNA or RNA libraries with approximately 10^{13}–10^{15} diversity through cycles of in vitro affinity selection and amplification known as SELEX (Systematic Evolution of Ligands by EXponential enrichment).[1,2] A counterselection is employed in the SELEX procedure to collect ssDNA or RNA sequences that only interact with target molecules, but not with control molecules. Consequently, aptamer candidates specifically binding to target molecules are enriched.

To date, hundreds of aptamers have been selected against different targets ranging from small molecules to live cells and are cataloged in an online database.[8] In most cases, aptamer selection has been performed using simple target molecules such as purified proteins (protein-SELEX). However, recent studies reported aptamer selection against complex targets, such as cell membrane proteins[9]

or whole cells (cell-SELEX). When investigating molecular probes for cancer, cell-SELEX has advantages over protein-SELEX. First, there is no need to purify and immobilize molecular targets and target molecules can maintain native folding and glycosylation states at the surface of cells.[10,11] Moreover, new molecular probes can be obtained even without prior knowledge of potential target molecules of cancer cells.[12] There have been several reports on cell-SELEX-based selection of aptamers against cancer cells, such as leukemia,[13–15] liver,[16] lung,[17–19] glioma,[20,21] colon,[22] and ovarian[23] cells.

Research group of Tan et al. isolated the ssDNA aptamer that recognizes mouse liver cancer cells by cell-SELEX;[16] and demonstrated that one of the isolated ssDNA aptamer also recognize human liver cancer cells.[24] However, no information was given on which sequence was important for specific binding to human liver cancer cells. In the present study, some ssDNA aptamers recognizing human liver cancer cells are directly isolated by the cell-SELEX using human hepatoma HepG2 cells as targets and human normal hepatocyte cells as counterparts, in order to extract the consensus sequence. Furthermore, we discuss the relationship between predicted secondary structure of the isolated aptamers and the binding affinity, and find the important consensus sequence and secondary structure in the isolated aptamers, which is responsible to the recognition of human liver cancer cells.

To monitor the enrichment of ssDNA aptamer candidates during cell-SELEX cycles, flow cytometric analysis was conducted for HepG2 cells (target cells) incubated with the FITC-labeled ssDNA

* Corresponding author. Tel.: +81 76 234 4807; fax: +81 76 234 4829.
E-mail address: nshimizu@t.kanazawa-u.ac.jp (N. Shimizu).

Table 1
Sequences of isolated ssDNA aptamers and their binding affinities toHepG2 cells

Sequence of random region (50 nt)	Group	Subgroup	Name	Percent in 11th round enriched pool [%]	Dissociation constant, K_d [nM]
TAACTCAATAAGCTAGGTGGGTGGGGGACACTACCCGGGGGTGGTTGGGT	I	A	A-1	28.8	450 ± 360
CAACTCAATAAGCTAGGTGGGTGGGGGACACTACCCGGGGGTGGTTGGGT		A	A-2	8.8	214 ± 82
TAACTCAATAAGCTAGGTGGGTGGGGGACACTGCCCGGGGGTGGTTGGGT		B	B-1	17.6	111 ± 41
CAACTCAATAAGCTAGGTGGGTGGGGGACACTGCCCGGGGGTGGTTGGGT		B	B-2	4.4	27 ± 1
TAACTCAATAAGCTAGGTGGGTGGGGGACACTATCCGGGGGTGGTTGGGT		C	C-1	8.8	20 ± 8
TAACTCAATAAGCTAGGTGGGTGGGGGACACTACTCGGGGGTGGTTGGGT		C	C-2	4.4	19 ± 1
CAACTCAATAAGCTAGGTGGGTGGGGGACACTACTCGGGGGTGGTTGGGT		C	C-3	2.2	50 ± 21
TAACTCAGTAAGCTAGGTGGGTGGGGGACACTATCCGGGGGTGGTTGGGT		C	C-4	2.2	141 ± 59
TAACTCAATAGGCTAGGTGGGTGGGGGACACTACCAGGGGGTGGTTGGGT		D	D-1	4.4	195 ± 131
CGATGGCGGTGGGTGGGGGACAAATTTGGGGGGCGTTGGGTGTTTGTGGT	II	E	E-1	11.1	64 ± 10
GGTGGTGGGGAGGGGGTTGCTGGGTCGCGACTAGGAAACTCATGCGGTAA	III	F	F-1	4.4	370 ± 311
TTCCGCAATGGCCCTCGATTACTGTCCCTACCACATGAGTTTCCCACATC	IV	G	G-1	2.2	153 ± 52

Underlined nucleotides in the sequence of group I indicate residues that differ from A-1.
Nucleotides marked with red and blue color indicated the consensus sequences.
The K_d values are the mean ± standard error obtained from three independent experiments.
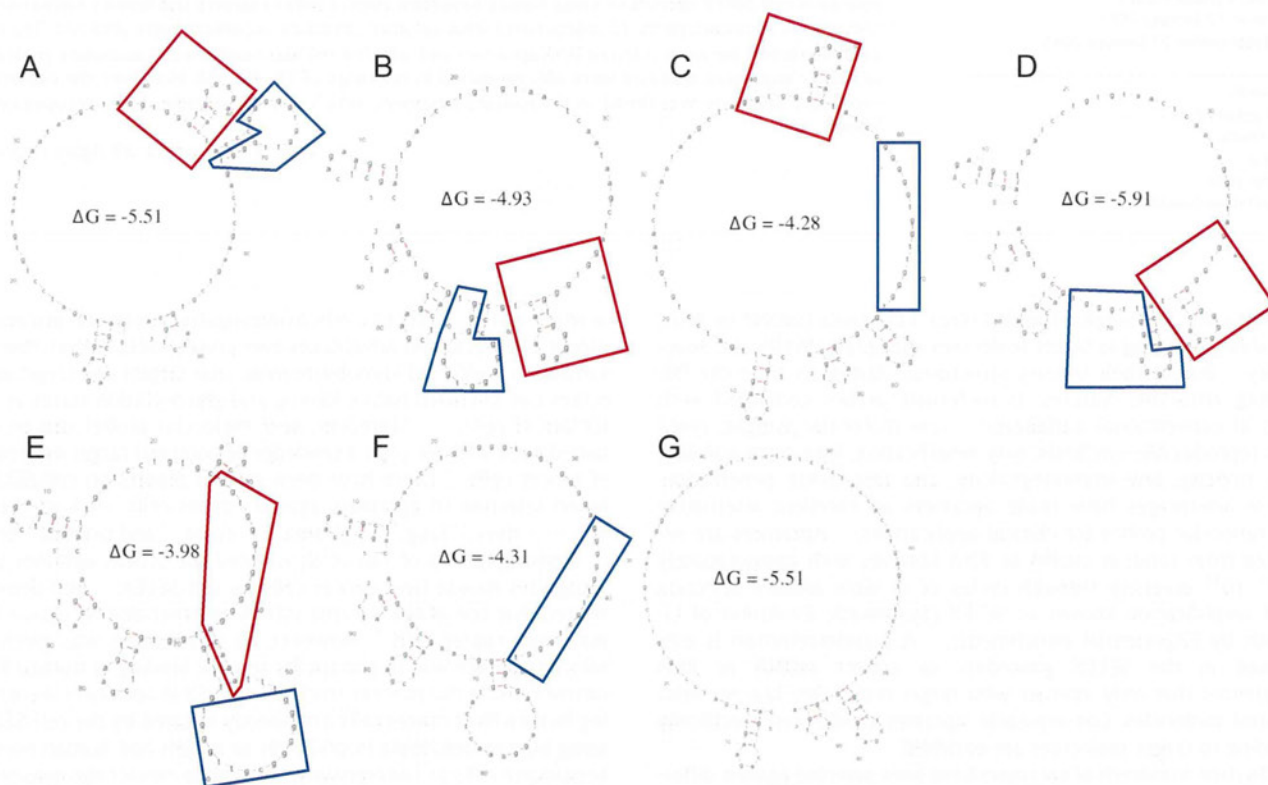
Figure 1. Secondary structures of ssDNA aptamers predicted by mfold software.[26] Letters (A–G) correspond to the aptamer subgroups listed in Table 1. The secondary structures marked with red and blue rectangles correspond to the sequences marked with red and blue text in Table 1. The numbers within the secondary structures indicate free energy changes calculated by the software.

pool obtained from various rounds of cell-SELEX (see references and notes for the detailed experimental procedures[25]). The peak of the histogram was shifted to a higher fluorescent intensity as cell-SE-LEX proceeded up to round 7, and no further enhancement of the fluorescent signal was observed from rounds 8–11 (see Fig. S2A).

This indicates that ssDNA aptamers with higher affinity to HepG2 cells were enriched by the first 7 rounds of cell-SELEX. On the other hand, when normal hepatocytes (counter cells) were incubated with the FITC-labeled ssDNA pool obtained from round 11, there was no substantial difference in the fluorescent histogram com-

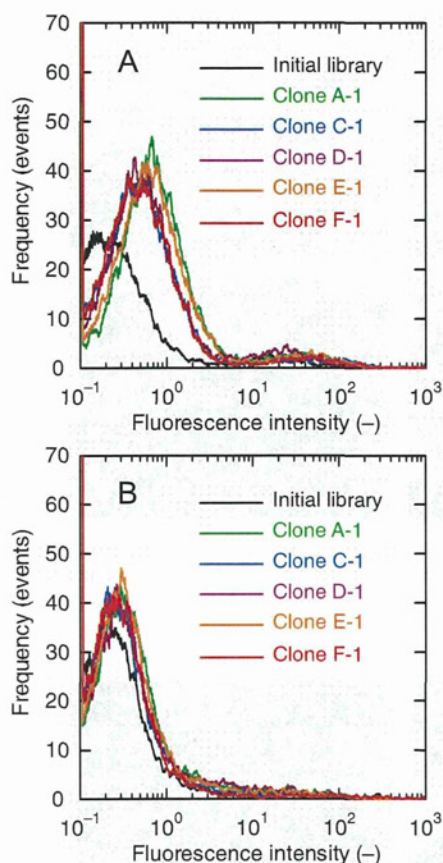**Figure 2.** Flow cytometry histogram of HepG2 cells (target cells, A) and normal hepatocytes (counter cells, B). The cells were incubated with the FITC-labeled ssDNA aptamer isolated after cell-SELEX rounds. Final concentration of the ssDNA aptamer was 200 nM in binding buffer.

pared with the initial ssDNA library (see Fig. S2B). These results indicate that the ssDNA aptamers specifically recognizing HepG2 cells could be enriched by the cell-SELEX procedure employed in this study. To confirm specific binding of the enriched ssDNA pool to target cells, fluorescent microscopy analysis was performed on HepG2 cells incubated with the FITC-labeled ssDNA pool from round 11 of cell-SELEX. Bright fluorescence was observed in HepG2 cells (Fig. S3B; target cells), while there was no fluorescence in normal hepatocytes (Fig. S3D; counter cells). Thus, individual ssDNA aptamer clones were isolated from the ssDNA pool obtained by round 11 of cell-SELEX.

After 11 rounds of cell-SELEX, the enriched aptamer pools were cloned and sequenced. Twelve independent aptamer sequences were obtained (Table 1) and they were categorized into 4 groups (I, II, III, and IV) based on sequence similarities. Group I made up 82.2% of the ssDNA pool after 11 rounds of cell-SELEX. Group I was further categorized into 4 subgroups (A–D) based on the secondary structures predicted by mfold software[26] (available at http://www.bioinfo.rpi.edu/applications/mfold/). Namely, 12 independent aptamer sequences were categorized into 7 subgroups (A–G). The estimated secondary structures of the 7 subgroups are shown in Figure 1.

To test the specific binding of the isolated ssDNA aptamers to target cells, flow cytometric analysis was conducted on HepG2 cells (target cells) incubated with the FITC-labeled ssDNA aptamer. Figure 2A shows the fluorescent histogram of representative ssDNA aptamer sequences. Irrespective of the aptamer sequences, the

peak of the histograms were similarly shifted to the higher fluorescent intensity compared with cases using the initial ssDNA library. By contrast, when the normal hepatocytes (counter cells) were incubated with the FITC-labeled ssDNA aptamer, the fluorescent histogram overlapped with cases using the initial ssDNA library (Fig. 2B). Thus, isolated ssDNA aptamers could specifically recognize HepG2 cells. To confirm specific binding of isolated ssDNA aptamers to target cells, fluorescent microscopy analysis was performed on HepG2 cells incubated with FITC-labeled ssDNA. As shown in Figure 3A–C, bright fluorescence was observed in HepG2 cells irrespective of the aptamer sequence used, while there was no fluorescence in normal hepatocytes (Fig. 3D–F; counter cells). Thus, the isolated ssDNA aptamer was specifically attached to HepG2 cells.

To evaluate binding affinity of the isolated ssDNA aptamer to target cells, the binding assay was conducted for the 12 sequences obtained (see Fig. S4), and K_d values were determined. As listed in Table 1, the K_d values of the 12 sequences obtained were in the range of 19–450 nM. The lowest K_d values were found in subgroup C out of the 7 subgroups listed in Table 1.

The ssDNA aptamer recognizing liver cancer cells had been isolated by Shangguan et al. using the cell-SELEX method with mouse liver cancer cells as targets and mouse normal cells as counterparts.[16] The isolated aptamer could specifically recognize mouse liver cancer cells, and also differentiated human liver cancer cells and normal cells.[24] In the present study, ssDNA aptamers that recognized human hepatoma HepG2 cells was isolated. The K_d value of the isolated aptamer was found to be 19 nM, which was similar to that of the reported aptamer recognizing human liver cancer cells (7.2 nM)[24] and to that of general antibodies. No similarity in nucleotide sequence and the predicted secondary structure was found between the ssDNA aptamers reported in the previous study and that isolated in the present study.

After aptamer isolation via SELEX rounds, truncation of aptamer sequences with maintaining binding affinity is usually conducted to reduce the cost of chemical synthesis, decrease the risk of random degradation, and increase tissue penetration rate.[4,5] In general, the length of minimized aptamers ranges from 25 to 45 nucleotides. The minimum aptamer sequences that maintain binding functionality has been experimentally determined by trial and error. Recently, the minimum aptamer sequences have been determined based on consensus sequences or consensus secondary structures predicted for the isolated aptamers.[27,28]

In the present study, primary sequences of the 12 aptamers clones were analyzed, and two guanine-rich consensus sequences were found in groups I, II, and III, marked with red and blue text in Table 1. Each of the nine isolated aptamer sequences in group I had the same consensus sequences and only a few differences in nucleotides. However, the K_d values were quite different, and lower K_d values were mainly observed in subgroup C (Table 1). Therefore, the secondary structure of the isolated aptamers was predicted to discuss the relationship between aptamer binding affinity and predicted secondary structure.

Figure 1A–D revealed that even a few differences in nucleotides could result in different secondary structures of the aptamers in group I. The predicted structures marked with red and blue rectangles in Figure 1 correspond to the consensus sequences marked with red and blue text in Table 1. We found that all the predicted secondary structures in group I had a common loop-stem structure, marked with red rectangles in Figure 1A–D. Thus, this consensus loop-stem structure was considered to be a key motif for binding to HepG2 cells. On the other hand, consensus sequences marked with blue text in Table 1 resulted in the formation of different types of loop-stem structures near the consensus loop-stem structure, as shown in Figures 1A, B, and D. We speculated that these different types of loop-stem structures caused steric hin-
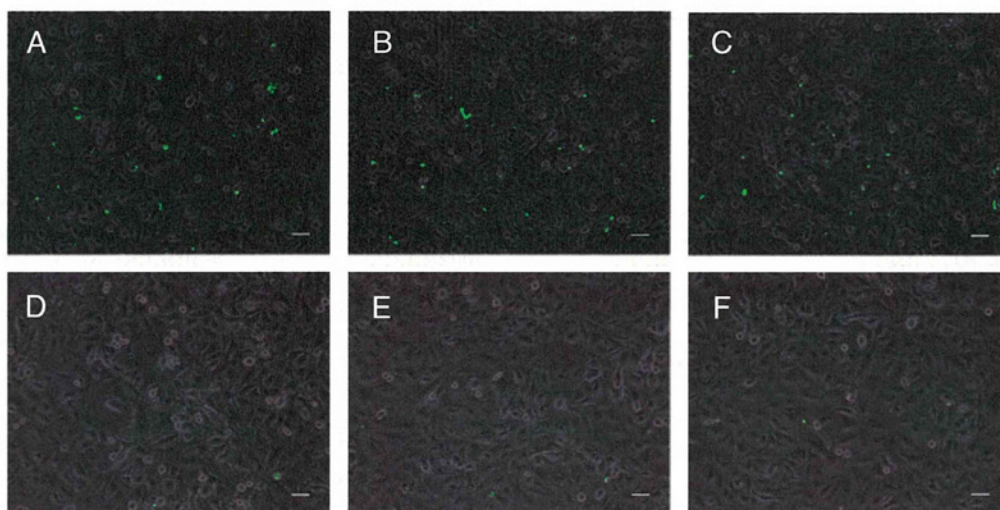
Figure 3. Fluorescent microscopic images of HepG2 cells (target cells, A, B, and C) and normal cells (counter cells, D, E, and F). The cells were incubated with the FITC-labeled ssDNA aptamer isolated after cell-SELEX rounds, that is, aptamer clone A-1 (A and D), aptamer clone C-1 (B and E), and aptamer clone D-1 (C and F). The images are overlays of fluorescent and bright-field images. Scale bars, 50 μm.
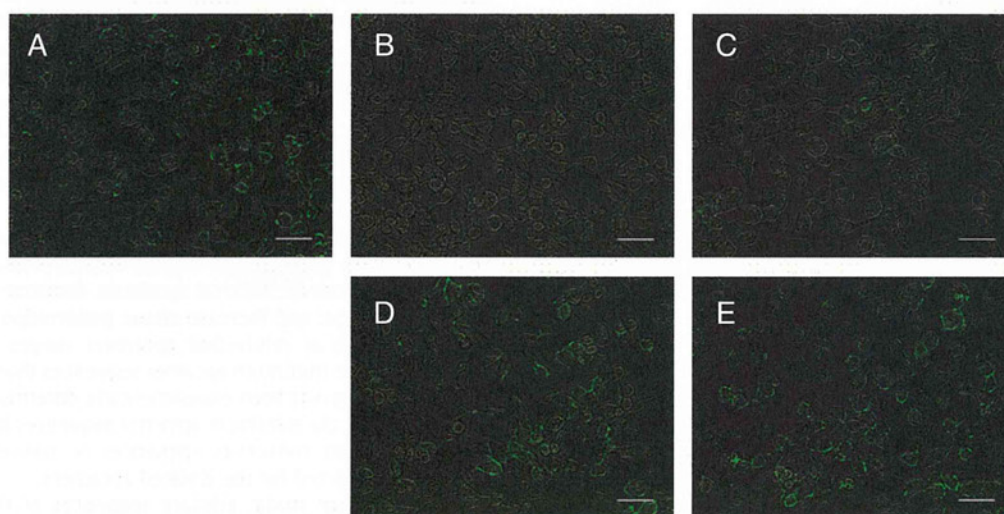

Figure 4. Fluorescent microscopic images of HepG2 cells (target cells) incubated with the FITC-labeled ssDNA aptamer. (A) Isolated ssDNA aptamer C-2; (B) ssDNA library C-2/N$_5$; (C) round 3 selected ssDNA pool; (D) round 5 selected ssDNA pool; and (E) round 7 selected ssDNA pool. The images are overlays of the fluorescent and bright-field images. Scale bars, 50 μm.

drance that limits the binding of the consensus loop-stem structures to their targets on HepG2 cell surfaces. This explains why the K_d values of subgroups A, B, and D were greater than those of subgroup C because no loop-stem structures were observed in the vicinity of the consensus loop-stem structures in subgroup C.

To examine the contribution of the consensus loop-stem structure marked with red rectangles in Figure 1C to the specific binding, randomization was introduced into the five nucleotides forming the loop structure (g-g-g-g-a) in the isolated ssDNA aptamer C-2. The randomization of these five nucleotides did not affect the predicted secondary structures of the isolated ssDNA aptamer C-2. (The resultant ssDNA pool was designated as C-2/N$_5$.) For evaluating the binding of the ssDNA pool C-2/N$_5$ to target cells, fluorescent microscopy analysis was performed on HepG2 cells incubated with the FITC-labeled ssDNA pool C-2/N$_5$. There was no fluorescence in the case of ssDNA pool C-2/N$_5$ (Fig. 4B), although the bright fluorescence was observed in the case of iso-

lated ssDNA aptamer C-2 (Fig. 4A). These results suggested the importance of the nucleotide sequence forming loop structure marked with red rectangles in Figure 1C for the specific binding to HepG2 cells.

Moreover, cell-SELEX was conducted again by using the ssDNA pool C-2/N$_5$ as initial library. (This procedure was designated as the 2nd cell-SELEX.) To monitor the enrichment of ssDNA aptamer candidates during the 2nd cell-SELEX cycles, fluorescent microscopic analysis was conducted for HepG2 cells (target cells) incubated with the FITC-labeled ssDNA pool obtained from various rounds of the 2nd cell-SELEX. As shown in Figure 4B–E, fluorescent signal on the images became larger as cell-SELEX proceeded up to round 7, and the fluorescent signal in the case of round 7 selected ssDNA pool was larger than that for the case of isolated ssDNA aptamer C-2 (Fig. 4E and A). This indicates that ssDNA aptamers with higher affinity to HepG2 cells than the isolated ssDNA aptamers C-2 were enriched by the 7 rounds of the 2nd cell-SELEX. Therefore, it was confirmed again that the

nucleotide sequence forming loop structure marked with red rectangles in Figure 1C was important for the specific binding to HepG2 cells. Moreover, it was suggested that the binding affinity of ssDNA aptamer against whole cancer cells can be further enhanced, by using both combinatorial screening of ligand (cell-SELEX) and rational determination of important sequence based on the prediction of consensus secondary structures.

In conclusion, ssDNA aptamers recognizing human hepatoma HepG2 cells were isolated using cell-SELEX. The K_d value was determined to be 19 nM, and the consensus sequence and secondary structure were found in the isolated aptamers, which was responsible to the responsible to the recognition of HepG2 cells. It is suggested that the minimum aptamer sequence that maintains binding affinity can be designed by extracting the consensus loop-stem structure mentioned above and elongating the stem structure to provide the aptamer with enough stability. As for aptamer-based cancer therapy, various types of targeted drug delivery systems (DDS) have been shown to achieve efficient and selective delivery of anticancer drugs to tumors. Typical examples include targeted DDS using drug–aptamer conjugates[29] and self-assembled nanovehicle–aptamer conjugates, such as liposomes,[30,31] micelles[32] and biodegradable polymers.[33] On the other hand, our previous study reported a new targeted DDS for cancer therapy that delivers titanium dioxide (TiO_2) nanoparticles to tumor tissues with subsequent generation of hydroxyl radicals from TiO_2 nanoparticles activated by external ultrasound irradiation.[34] The construction of the TiO_2 nanoparticle–aptamer conjugate will be able to provide sonodynamic cancer therapy with enhanced treatment specificity and efficacy.

Acknowledgments

Supplementary data

Supplementary data associated with this article can be found, in the online version, at http://dx.doi.org/10.1016/j.bmcl.2013.01.040.

References and notes

1. Ellington, A. D.; Szostak, J. W. *Nature* **1990**, *346*, 818.
2. Tuerk, C.; Gold, L. *Science* **1990**, *249*, 505.
3. Breaker, R. R. *Nature* **2004**, *432*, 838.
4. Jayasena, S. D. *Clin. Chem.* **1999**, *45*, 1628.
5. Hicke, B. J.; Stephens, A. W. *J. Clin. Invest.* **2000**, *106*, 923.
6. Tan, W.; Wang, H.; Chen, Y.; Zhang, X.; Zhu, H.; Yang, C.; Yang, R.; Liu, C. *Trends Biotechnol.* **2011**, *29*, 634.
7. Lee, J. F.; Stovall, G. M.; Ellington, A. D. *Curr. Opin. Chem. Biol.* **2006**, *10*, 282.
8. Lee, J. F.; Hesselberth, J. R.; Meyers, L. A.; Ellington, A. D. *Nucleic Acids Res.* **2004**, *32*, D95.
9. Morris, K. N.; Jensen, K. B.; Julin, C. M.; Weil, M.; Gold, L. *Proc. Natl. Acad. Sci. U.S.A.* **1998**, *95*, 2902.
10. Hicke, B. J.; Marion, C.; Chang, Y. F.; Gould, T.; Lynott, C. K.; Parma, D.; Schmidt, P. G.; Warren, S. *J. Biol. Chem.* **2001**, *276*, 48644.
11. Daniels, D. A.; Chen, H.; Hicke, B. J.; Swiderek, K. M.; Gold, L. *Proc. Natl. Acad. Sci. U.S.A.* **2003**, *100*, 15416.
12. Blank, M.; Weinschenk, T.; Priemer, M.; Schluesener, H. *J. Biol. Chem.* **2001**, *276*, 16464.
13. Shangguan, D.; Li, Y.; Tang, Z.; Cao, Z. C.; Chen, H. W.; Mallikaratchy, P.; Sefah, K.; Yang, C. J.; Tan, W. *Proc. Natl. Acad. Sci. U.S.A.* **2006**, *103*, 11838.
14. Tang, Z.; Shangguan, D.; Wang, K.; Shi, H.; Sefah, K.; Mallikratchy, P.; Chen, H. W.; Li, Y.; Tan, W. *Anal. Chem.* **2007**, *79*, 4900.
15. Sefah, K.; Tang, Z. W.; Shangguan, D. H.; Chen, H.; Lopez-Colon, D.; Li, Y.; Parekh, P.; Martin, J.; Meng, L.; Phillips, J. A.; Kim, Y. M.; Tan, W. H. *Leukemia* **2009**, *23*, 235.
16. Shangguan, D.; Meng, L.; Cao, Z. C.; Xiao, Z.; Fang, X.; Li, Y.; Cardona, D.; Witek, R. P.; Liu, C.; Tan, W. *Anal. Chem.* **2008**, *80*, 721.
17. Chen, H. W.; Medley, C. D.; Sefah, K.; Shangguan, D.; Tang, Z.; Meng, L.; Smith, J. E.; Tan, W. *ChemMedChem* **2008**, *3*, 991.
18. Zhao, Z.; Xu, L.; Shi, X.; Tan, W.; Fang, X.; Shangguan, D. *Analyst* **1808**, *2009*, 134.
19. Kunii, T.; Ogura, S.; Mie, M.; Kobatake, E. *Analyst* **2011**, *136*, 1310.
20. Cerchia, L.; Esposito, C. L.; Jacobs, A. H.; Tavitian, B.; De Franciscis, V. *PLoS One* **2009**, *4*, e7971.
21. Bayrac, A. T.; Sefah, K.; Parekh, P.; Bayrac, C.; Gulbakan, B.; Oktem, H. A.; Tan, W. *ACS Chem. Neurosci.* **2011**, *2*, 175.
22. Sefah, K.; Meng, L.; Lopez-Colon, D.; Jimenez, E.; Liu, C.; Tan, W. *PLoS One* **2010**, *5*, e14269.
23. Van Simaeys, D.; López-Colón, D.; Sefah, K.; Sutphen, R.; Jimenez, E.; Tan, W. *PLoS One* **2010**, *5*, e13770.
24. Meng, L.; Yang, L.; Zhao, X.; Zhang, L.; Zhu, H.; Liu, C.; Tan, W. *PLoS One* **2012**, *7*, e33434.
25. Human hepatoma HepG2 cells, used as target cells for cell-SELEX, were purchased from RIKEN cell bank (Tsukuba, Japan). Primary normal human liver hepatocyte cells, used as counterparts of HepG2 cells, were purchased from DS Pharma Medical Co. Ltd (Osaka, Japan). HepG2 cells were cultured in Dulbecco's modified Eagle's medium (DMEM; Nakarai Tesqu, Kyoto, Japan) supplemented with 10% (v/v) fetal bovine serum (FBS; Invitrogen GIBCO, Carlsbad, CA, USA). Normal hepatocyte cells were cultured in a medium prepared by CSC complete medium kit R (DS Pharma Medical Co. Ltd, Osaka, Japan). In both cases, media were supplemented with 100 U/ml penicillin, 100 µg/ml streptomycin, and 0.25 µg/ml amphotericin B (Nakarai Tesqu). Cells were maintained at 37 °C under 5% CO_2 atmosphere.
For cell-SELEX, 1×10^6 cells suspended in 5 ml medium were seeded in 60-mm collagen type I coated culture dish (AGC Techno Glass Co. Ltd, Tokyo, Japan) and incubated for 48 h up to approximately 2×10^6 cells. The cell monolayer adhered to the dish was washed thrice with Dulbecco's phosphate buffered saline with calcium chloride and magnesium chloride (D-PBS(+)) before addition of the ssDNA pool or isolated ssDNA aptamer. Binding buffer used for dissolution of ssDNA was D-PBS(+) supplemented with 1 mg/ml bovine serum albumin (BSA; Nakarai Tesqu), unless otherwise noted.
The ssDNA library contained a central randomized sequence of 50 nucleotides (nt) flanked by 23- and 22-nt primer hybridization sites (5′-CAGCTCA GAAGCTTGATCCTGTG-50nt-GACTCGAAGTCGTGCATCTGCA-3′). A fluorescein isothiocyanate (FITC)-labeled sense primer (5′-FITC-CAGCTCAGA AGCTTGAT CCTGTG-3′) and a biotinylated (Bio) antisense primer (5′-Bio-TGCAGATGCA CGACTTCGAGTC-3′) were used in PCR for the synthesis of double-labeled, double-stranded DNA (dsDNA) molecules. These oligonucleotides were synthesized and purified by reverse phase HPLC (Operon Biotechnologies, Tokyo, Japan).
As shown in Figure S1, a round of the cell-SELEX procedure consisted of (i) negative selection using counter cells, (ii) positive selection using target cells, (iii) elution of ssDNA from the target cells, (iv) PCR amplification of dsDNA, and (v) separation of ssDNA for the next round of cell-SELEX. Prior to negative selection, 200 pmol of the ssDNA pool dissolved in 500 µl of the binding buffer was denatured by heating at 95 °C for 5 min and refolded by cooling on ice for 10 min. Moreover, the refolded ssDNA pool was incubated in the empty culture dish at 37 °C for 45 min and recovered. (i) For negative selection, the prepared ssDNA pool (400 nM) was incubated with the normal hepatocyte cell monolayer on the dish (counter cells) at 37 °C for 45 min in the CO_2 incubator. A supernatant containing the unbound ssDNA was recovered and used for a subsequent positive selection step. (ii) The recovered ssDNA pool was incubated with HepG2 cell monolayer on the dish (target cells) at 37 °C for 45 min in the CO_2 incubator. To remove ssDNA not bound to HepG2 cells, the dish was washed twice with 2 ml of the binding buffer, unless otherwise noted. (iii) For elution of ssDNAs bound to the target, HepG2 cell monolayer was harvested by enzymatic treatment at 37 °C for 3 min using 500 µl of trypsin–EDTA solution (2.5 g/l trypsin and 1 mM EDTA-2Na in D-PBS(−); Nakarai Tesqu, Kyoto, Japan). The harvested cell suspension was heated at 95 °C for 10 min to elute the bound ssDNA from the cell surface. The eluted ssDNA solution was serially filtered with 0.45 µm and 0.22 µm micro membrane to remove cell debris, and then desalted by ethanol precipitation. (iv) The eluted ssDNA was amplified by PCR with FITC-labeled sense primers and biotin-labeled antisense primers (2 min at 94 °C, followed by 15 cycles of 15 s at 94 °C, 15 s at 55 °C, and 30 s at 72 °C, followed by 10 min at 72 °C); *Taq* polymerase and dNTPs were obtained from Toyobo Co Ltd, Osaka, Japan). (v) FITC-labeled sense ssDNA was separated from the biotinylated antisense ssDNA strand using streptavidin-coated Sepharose beads (Streptavidin HP Spin Trap; GE Healthcare, Tokyo Japan) and denaturation in alkaline conditions (0.2 M NaOH). After neutralization and desalination, the recovered FITC-labeled ssDNA pool was used for the next round of cell-SELEX or to monitor the progression of cell-SELEX by flow cytometry.
The negative selection step was skipped during rounds 1–7 of the cell-SELEX procedure. To decrease non-specific binding, the binding buffer was supplemented with 20% FBS and 1 mg/ml BSA after round 6. Moreover, to acquire aptamers with high affinity, the wash strength in the positive selection step was gradually enhanced by increasing the number of washes (from 2 to 5) and the volume of wash buffer (from 2 to 5 ml). After 11 rounds of cell-SELEX, the selected ssDNA pool was PCR amplified using unmodified primers and cloned into *Escherichia coli* using the TA cloning kit (Takara Bio Inc., Shiga, Japan). Clones were sequenced by standard automated DNA sequencing methods.
Flow cytometric analysis was performed to monitor the enrichment of aptamer candidates in the initial ssDNA library during cell-SELEX rounds or to test the binding affinity of isolated ssDNA aptamers to target cells. HepG2 and normal

hepatocyte cell monolayers were detached using non-enzymatic cell dissociation solution (Takara) because enzymatic cell dissociation using trypsin could cleave cell surface proteins to which aptamers bind. After washing twice with D-PBS(+), 3×10^5 cells were incubated with 200 µl of the FITC-labeled ssDNA pool (200 nM) or FITC-labeled ssDNA aptamers (0–200 nM) in the binding buffer at RT for 30 min in the dark. The cells were then washed twice with binding buffer and suspended in 300 µl of binding buffer. The fluorescent signal from the cells was detected using a flow cytometer (EPICS XL-MCL ADC, Beckman Coulter, Inc., Brea, CA USA) by counting 5000 events. The FITC-labeled initial ssDNA library was also used as a negative control.

In evaluating the binding affinity of isolated ssDNA aptamers to target cells, mean fluorescent intensity was determined from the flow cytometry histogram data. Here, the mean fluorescence intensity determined using the initial ssDNA library at corresponding concentrations was regarded as signal caused by non-specific binding and was subtracted from the mean fluorescence intensity obtained using the isolated ssDNA aptamers. The equilibrium dissociation constant (K_d) of the aptamer–cell interaction was determined by fitting the following equation to the relationship between mean fluorescence intensity of specific binding (F) and aptamer concentration (C_A) using the non-linear least square method.

$$F = F_{max} \, C_A/(K_d + C_A)$$

Experiments for determination of the K_d value were replicated thrice.

26. Zuker, M. *Nucleic Acids Res.* **2003**, *31*, 3406.
27. Shangguan, D.; Tang, Z.; Mallikaratchy, P.; Xiao, Z.; Tan, W. *ChemBioChem* **2007**, *8*, 603.
28. Bing, T.; Yang, X.; Mei, H.; Cao, Z.; Shangguan, D. *Bioorg. Med. Chem.* **2010**, *18*, 1798.
29. Huang, Y. F.; Shangguan, D.; Liu, H.; Phillips, J. A.; Zhang, X.; Chen, Y.; Tan, W. *ChemBioChem* **2009**, *10*, 862.
30. Cao, Z.; Tong, R.; Mishra, A.; Xu, W.; Wong, G. C. L.; Cheng, J.; Lu, Y. *Angew. Chem., Int. Ed.* **2009**, *48*, 6494.
31. Kang, H.; O'Donoghue, M. B.; Liu, H.; Tan, W. *Chem. Commun. (Camb.)* **2010**, *46*, 249.
32. Wu, Y.; Sefah, K.; Liu, H.; Wang, R.; Tan, W. *Proc. Natl. Acad. Sci. U.S.A.* **2010**, *107*, 5.
33. Farokhzad, O. C.; Cheng, J.; Teply, B. A.; Sherifi, I.; Jon, S.; Kantoff, P. W.; Richie, J. P.; Langer, R. *Proc. Natl. Acad. Sci. U.S.A.* **2006**, *103*, 6315.
34. Ninomiya, K.; Ogino, C.; Oshima, S.; Sonoke, S.; Kuroda, S.; Shimizu, N. *Ultrason. Sonochem.* **2012**, *19*, 607.
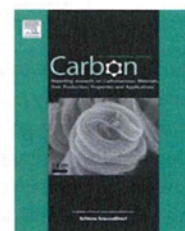
Sidewall modification of multiwalled carbon nanotubes by *Allivum sativum* (garlic) and its effect on the deposition of gold nanoparticles

Sarvesh Kumar Srivastava [a], Ryosuke Yamada [b], Chiaki Ogino [a], Akihiko Kondo [a,*]

[a] Department of Chemical Science and Engineering, Graduate School of Engineering, Kobe University, 1-1 Rokkodai-cho, Nada, Kobe 657-8501, Japan
[b] Organization of Advanced Science and Technology, Kobe University, 1-1 Rokkodai-cho, Nada, Kobe 657-8501, Japan

ARTICLE INFO

ABSTRACT

Sidewall modification of multiwalled carbon nanotubes (abbreviated as MWCNTs) was achieved using *Allivum sativum* (garlic) extract by an acid-free green process. These organo-sulfur modified-MWCNTs were then decorated with gold nanoparticles and examined by transmission electron microscopy. The presence of organosulfurs over the modified nanotube surface was confirmed. Nanotube surface modification and subsequent presence of thiols as an active linker was confirmed by Raman spectroscopy, Fourier transform infrared spectroscopy, energy dispersive X-ray and X-ray photoelectron spectroscopy. In the absence of these organosulfurs (thiols), no gold nanoparticle attachment was observed. Both small (1–8 nm) and large (12–20 nm) gold nanoparticles were found to decorate the modified nanotube surface suggesting coalescence among nanoparticles.

© 2013 Elsevier Ltd. All rights reserved.

1. Introduction

In recent years, nanoscience and nanotechnology has made considerable progress towards synthesis and characterization of new materials due to their wide-spread application in everyday life. Much of this success was possible due to chemical modifications or functionalization of carbon nanotube (CNT) surface [1]. This combination of chemically modified nanotubes decorated with nanoparticles has found tremendous usage in electronics, sensors, biomedical applications, catalysis, H_2 storage, etc. [2]. Gold nanoparticles (Au NPs) in particular, happens to be a key material and building block for newer technologies owing to their unique set of properties at nanoscale [3]. Several methods for functionalizing CNTs followed by Au NP deposition on the modified nanotube surface were proposed recently. Satishkumar et al. [4] showed that CNTs upon harsh acid treatment allowed tagging of metal nanoparticles (including Au NPs) on the modified nano-

tube surface. Also, Jiang et al. [5] showed selective attachment of Au NPs on nitrogen-doped multi-walled carbon nanotubes (MWCNTs) with H_2SO_4–HNO_3 chemical treatment. Similarly, surface activation by carboxylic acid [6] and thio-amide-carboxyl [7] surface has been reported for immobilization of metal NPs. The general idea which prevailed was that pristine CNTs are inert structures and harsh pre-treatment is needed to create 'openings' on the CNT surface for attaching other chemical groups. However, Ellis et al. [8] demonstrated weak hydrophobic anchoring of Au NPs by utilizing thiol capping on acetone (–OH group) activated CNT surface. Similarly, other techniques were also reported [9–11] for Au NP attachment on CNT surface. However, most of these techniques were without any chemical modification of nanotube surface thereby limiting the binding strength and capacity of Au NPs over the nanotube surface. Since, CNTs are not ideal structures and contain defect sites and impurities [12], this makes them ideal site for addition reactions [13]. These defect sites

can be exploited to tag metal nanoparticles onto the CNT surface without any harsh treatment as demonstrated by Zanella et al. [14] to tag gold nanoparticles via thiol linkages [15–17]. These sulfur linkages when attached to the defect sites, open new possibilities for attaching other chemical groups (including nanoparticles) at the vacancy defect sites. Although, considerable efforts have been made in pre-treatment of CNTs as discussed previously, most of these techniques require excessive usage of toxic solvents, acid pre-treatment and rigorous process control at high temperatures. Thus, there is a need to functionalize CNTs in a more benign and eco-friendly manner. With this aim, we hereby provide a novel biogenic method for CNT surface thiolation and subsequent attachment of Au NPs by utilizing organosulfur plant extract. Garlic is one such natural source of organosulfur compounds [18] where total sulfur content ranges from 0.35% to 1% of its dry weight [19]. Here, we report CNT surface modification by utilizing natural organosulfurs from *Alllium sativum* (Garlic) and its effect on the deposition of Au NPs onto the modified CNT surface under ambient reaction conditions with an acid-free green process. This biogenic study has the potential to evolve into biomimetic study with advanced interdisciplinary research to provide innovative surface modification strategies for carbonaceous materials in future.

2. Experimental

2.1. CNT surface modification

Prepared MWCNTs from chemical vapor deposition (CVD) process (Aldrich, USA; 95% purity, 6–9 nm; 5 μm) were used. CNT surface modification was carried out by freshly chopped garlic (100 g) cloves, which were crushed and extracted with 20 mL aqueous solution of water:ethanol (95:5 v/v). This extract was centrifuged at $3500g$ to remove any suspended solids and the supernatant was retained. It is important to note that 80% of organosulfurs in garlic cloves convert to allicin (diallyl thiosulfinate) by enzymatic activity of allinase (naturally present in garlic) which converts alliin (3-(2-propenylsulfinyl)alanine) upon being cut in the presence of water in a period of 10–15 s [20]. At elevated temperatures, alliin rapidly converts to diallyl trisulfide (DATS) and diallyl disulfite [21]. Since, CNT sidewall functionalization is affected with the curvature of carbon nanotubes [22], we preferred small diameter MWCNTs for thermal activation in plastic vials by solvent-free process [23] of baking reactant mixture at elevated temperature. MWCNTs (10 mg) were placed together with organosulfur extract (2 mL, 80 mg dry weight) and heated at 110 °C for 4 h in sealed vials. This reaction mixture was sonicated for 15 s at every hour to homogenize the reaction solution. Excess of organosulfur extract was removed from the reaction mixture by centrifugation at $3500g$ for 2 min. Finally, organosulfur modified multi-walled nanotubes (to be referred as OS-MWCNT) was obtained.

2.2. Decoration of gold nanoparticles on CNTs

Gold nanoparticles were prepared by the reaction of $HAuCl_4$ (Sigma) and citric acid (Aldrich). In a typical experiment,

5 mg of OS-MWCNT was dispersed in 1-butanol (5 mL) and sonicated for 10 min. Then, 0.016 g of $HAuCl_4$ and 0.017 g citric acid, both dissolved separately in 5 mL of 1-butanol were stirred for 30 min to produce Au NPs [24] before being added dropwise into the dispersion of OS-MWCNTs. Final volume was set to 10 mL. This dispersion was vigorously stirred at room temperature for 3 h with intermittent sonication of 15 s at every 30 min. After this procedure, solid phase was separated by centrifugation ($3500g$ for 10 min) and washed six times with 1-butanol to remove any non-linking Au NP from the CNT surface. Finally, we obtained our desired product of OS-MWCNTs decorated with Au NPs (Au-OS-MWCNT) which were dried at 60 °C and stored away from light in a vacuum desiccator. As a control test, same procedure of Au NP deposition was performed with pristine MWCNTs.

2.3. Characterization of Au-CNT nanocomposite

Preliminary analysis of Au NP deposition over the modified CNT surface was done by NanoDrop 3300 Fluorospectrometer operated at 400–600 nm with relative fluorescence units (RFU) at 540 nm. MWCNTs – with and without Au NP attachment dispersed in 1-butanol were transferred to carbon coated grid for transmission electron microscopy (TEM) measurements by Hitachi H-7100 transmission electron microscope and Jeol JEM 1011 electron microscope operated at 100 and 200 kV, respectively. Images obtained were analyzed using ImageJ 1.43M software. Transmission mode Fourier transform infrared (FT-IR) spectroscopy was carried out using Jasco FTIR-680 plus coupled to a high performance computer. The results reported here were obtained from 200 scans at a 4 cm^{-1} resolution and were verified five times with different nanocomposite samples prepared and stored under identical conditions. Energy dispersive X-ray (EDX) analysis was done to confirm sulfur linkages present over the nanotube surface using JEOL JSM6400 operating at an accelerating voltage of 15 kV and working distance of 15 mm; resulting spectra were analyzed using Spectra Manager ver. 1.06.02. Raman spectra was obtained by using the 514.5 nm line of an Ar$^+$ laser (100 mW) analyzed by a JOBIN-YVON monochromator Model U-1000 for 10 cycles each of 16 s. Confirmatory analysis for sidewall addition of thiol onto CNT surface was done by X-ray photoelectron spectroscopy (XPS) obtained from JEOL JPS9010 MC photoelectron spectrometer operating at 10 kV and 30 mA. The results obtained were analyzed by SpecSurf ver. 1.7.3.9 software.

3. Results and discussion

Fig. 1a shows fluorospectra of OS-MWCNT decorated with Au NPs and spectra of Au NPs alone (Fig. 1b).

Both samples showed distinct surface plasmon resonance peak (SPR) at 540 nm when laser excitation was made in the white light region. This characteristic absorbance at 520–540 nm suggest towards the presence of gold nanoparticles linked over the modified CNT surface. The SPR peak remained after repeated washing and vigorous sonication. This preliminary result indicated that Au NPs may be attached onto the modified nanotube surface. Also, retention